

CORE-COLLAPSE SUPERNOVA EXPLOSIONS TRIGGERED BY A QUARK-HADRON PHASE TRANSITION DURING THE EARLY POST-BOUNCE PHASE

T. FISCHER^{1,2,3}, I. SAGERT⁴, G. PAGLIARA⁵, M. HEMPEL³, J. SCHAFFNER-BIELICH⁵, T. RAUSCHER³, F.-K. THIELEMANN³,
R. KÄPPELI³, G. MARTÍNEZ-PINEDO¹ AND M. LIEBENDÖRFER³

¹ GSI, Helmholtzzentrum für Schwerionenforschung GmbH, Planckstraße 1, 64291 Darmstadt, Germany

² Technische Universität Darmstadt, Schlossgartenstraße 9, 64289 Darmstadt, Germany

³ Department of Physics, University of Basel, Klingelbergstraße 82, 4056 Basel, Switzerland

⁴ Department of Physics & Astronomy, Michigan State University, East Lansing, MI 48824, U.S.A

⁵ Institut für Theoretische Physik, Ruprecht-Karls-Universität, Philosophenweg 16, 69129 Heidelberg, Germany

(Dated: May 23, 2018)
Draft version May 23, 2018

ABSTRACT

We explore explosions of massive stars, which are triggered via the quark-hadron phase transition during the early post bounce phase of core-collapse supernovae. We construct a quark equation of state, based on the bag model for strange quark matter. The transition between the hadronic and the quark phases is constructed applying Gibbs conditions. The resulting quark-hadron hybrid equations of state are used in core-collapse supernova simulations, based on general relativistic radiation hydrodynamics and three flavor Boltzmann neutrino transport in spherical symmetry. The formation of a mixed phase reduces the adiabatic index, which induces the gravitational collapse of the central proton-neutron star. The collapse halts in the pure quark phase, where the adiabatic index increases. A strong accretion shock forms, which propagates towards the proton-neutron star surface. Due to the density decrease of several orders of magnitude, the accretion shock turns into a dynamic shock with matter outflow. This moment defines the onset of the explosion in supernova models that allow for a quark-hadron phase transition, where otherwise no explosions could be obtained. The shock propagation across the neutrinospheres releases a burst of neutrinos. This serves as a strong observable identification for the structural reconfiguration of the stellar core. The ejected matter expands on a short timescale and remains neutron-rich. These conditions might be suitable for the production of heavy elements via the r -process. The neutron-rich material is followed by proton-rich neutrino-driven ejecta in the later cooling phase of the proton-neutron star where the νp -process might occur.

Subject headings: equation of state – dense matter – gravitation – shock waves – supernovae – neutron stars

1. INTRODUCTION

The explosion mechanism of massive stars is an active subject of research in theoretical astrophysics. In this article, we explore a scenario where the explosion is triggered due to the phase transition from hadronic matter to quark matter. We present specific and distinguished characteristics for possible explosion observables.

Stars with an initial main sequence mass above $10 M_{\odot}$ produce extended Fe-cores, as the end product of nuclear burning. During the following evolution, the photodisintegration of heavy nuclei as well as electron captures reduce the pressure of the Fe-core. The initial contraction of the core proceeds into a collapse, during which density and temperature rise. At nuclear densities the repulsive nuclear interaction causes a significant stiffening of the equation of state (EoS), which in turn leads to the formation of a shock wave. As it propagates outward it continuously loses energy due to the dissociation of in-falling heavy nuclei from the progenitor. The central object formed at core bounce is a hot and lepton-rich proton-neutron star (PNS). The shock propagation across the neutrinospheres, i.e. the neutrino energy and flavor dependent spheres of last scattering, releases a burst of electron neutrinos - known as the deleptonization burst - emitted from electron capture at free protons. The electron neutrino luminosity rises up to several 10^{53} erg/s (depending on the progenitor) on a timescale of 5–20 ms

after bounce. This enormous energy loss, in combination with the dissociation of the in-falling heavy nuclei, turns the dynamic shock into a standing accretion shock (SAS) already at about 5 ms after bounce (see e.g. Hillebrandt & Müller 1981; Mayle & Wilson 1987; Bruenn 1989; Myra & Bludman 1989). The deleptonization near the neutrinospheres results in a low proton-to-baryon ratio (given by the electron fraction) of $Y_e = 0.1$ – 0.2 . The PNS interior, which did not experience shock heating, stays slightly less neutron-rich where $Y_e \simeq 0.3$ at bounce (depending on the equation of state and the electron capture rates).

In an attempt to explain core-collapse supernova explosions, neutrino heating was suggested as a mechanism for the revival of the SAS by Bethe & Wilson (1985), leading to so called neutrino-driven explosions. In spherical symmetry, this mechanism has been shown to produce explosions only for the low mass $8.8 M_{\odot}$ O-Ne-Mg-core from Nomoto (1983,1984,1987) by Kitaura et al. (2006) and Fischer et al. (2010b). Multi-dimensional phenomena, such as rotation, convection and the development of fluid instabilities, have been shown to increase the neutrino heating efficiency (see e.g. Miller et al. 1993; Herant et al. 1994; Burrows et al. 1995; Janka & Mueller 1996). Such models help to aid the understanding of aspherical explosions (see also Bruenn et al. 2009; Marek & Janka 2009, and references therein). Besides

neutrino heating (Bethe & Wilson 1985), alternative explosive scenarios have been explored, such as the dumping of magnetic energy by LeBlanc & Wilson (1970), Moiseenko & Bisnovaty-Kogan (2007) and Takiwaki et al. (2009) as well as by acoustic energy by Burrows et al. (2006). The later two scenarios require multi-dimensional models.

An additional scenario is obtained by looking at the conditions achieved at the PNS interior during the post bounce phase of core-collapse supernovae. Due to the mass accretion on the order of several $0.1 M_{\odot}/s$, the central density rises above several times nuclear matter density and the temperature above several tens of MeV (depending on the progenitor model). With increasing degeneracy, the central electron fraction reduces below $Y_e \lesssim 0.25$ on timescales on the order of several 100 ms post bounce. The timescale for the PNS contraction depends on the mass accretion rate which in turn is in direct correlation with the progenitor model. The conditions obtained in the PNS interiors raise the question about the state of matter and possibly the appearance of exotic matter such as hyperons and quarks.

Assuming a purely hadronic composition, matter is composed of color charged quarks which cannot propagate freely and are confined into color neutral baryons and mesons. At high temperatures or baryon densities, hadronic matter is expected to change its state to a phase of deconfined quarks and gluons, where chiral symmetry is restored. Thereby, deconfinement and asymptotic freedom allow color charged quarks and gluons to move as free and almost non-interacting particles. Due to chiral symmetry restoration, the quarks obtain their current mass values, which for the up and down quarks are in the range of few MeV, while the strange quark current mass is about $m_s \sim 100$ MeV.

In Quantum Chromodynamics (QCD), which is believed to be the fundamental theory behind the strong force, the interaction of quarks is characterized by an effective coupling constant α_s , which monotonically approaches zero at large momentum transfer. For small values of α_s , a perturbative treatment of the strong interaction can be applied. However, at the energy scale of quark deconfinement, the interaction strength becomes too large and a perturbative treatment is no longer applicable, requiring alternative approaches. One possible description is the phenomenological quark bag model (see e.g. Detar & Donoghue 1983), based on the spatial confinement of quarks. In Nambu-Jona-Lasinio models, quarks are implemented as quantum fields with point-like interactions in a chirally symmetric Lagrangian (see Buballa 2005, and references therein). More advanced methods to describe quark matter are based on e.g. the Dyson-Schwinger equation (see Fischer 2006) or ab initio calculations of QCD on the lattice. Ab initio calculations show a smooth crossover from a hadronic phase to a deconfined quark gluon plasma phase, at high temperatures and low baryochemical potentials (see e.g. Fodor & Katz 2004; Aoki et al. 2006). On the other hand, field theoretical and phenomenological calculations point to a first order phase transition from hadronic to quark matter at large chemical potentials and finite temperatures (see Berges & Rajagopal 1999; Klevansky 1992; Pisarski & Wilczek 1984). The many open questions concerning critical temperatures and densities, the

order of the phase transition and whether both chiral symmetry restoration and deconfinement happen simultaneously or not, make QCD phase transitions an active topic of experimental research at the Relativistic Heavy Ion Collider (RHIC) in Brookhaven, the Large Hadron Collider (LHC) at CERN and the Facility for Antiproton and Ion Research (FAIR) at GSI, Darmstadt and at NICA in Dubna (Russia). The experiments at the LHC and RHIC are focused on the production of matter at high temperatures and low baryochemical potentials. On the other hand, FAIR and NICA will be designed to study nuclear matter at large densities and temperatures, which are conditions that correspond to core-collapse supernova interiors. They will enable a crosscheck of results from terrestrial experiments and astrophysical observations. However, the conditions in supernovae, neutron-rich matter and the possible production of strange quarks by weak interactions, differ from those in heavy-ion collision experiments. As will be discussed below, a quark-hadron phase transition at large baryon number densities in heavy-ion collisions can be compatible with low critical densities for the appearance of quark matter in supernovae and neutron stars. A detailed discussion of this issue will be given in § 2.

The first attempt to investigate the quark-hadron phase transition in simulations of massive stars goes back to Takahara & Sato (1988). They tried to find a connection between the appearance of quark matter and the apparent but statistically insignificant multi-peaked neutrino signal from SN1987a (see Hirata et al. 1988; Bionta et al. 1987), using general relativistic hydrodynamics in spherical symmetry and a polytropic EoS. More sophisticated input physics was applied in the investigation by Gentile et al. (1993). Their model was based on general relativistic hydrodynamics and a parametrized description of the deleptonization during the Fe-core collapse as well as an improved EoS for both hadronic and quark matter. The transition between these two phases was constructed via a co-existence region, i.e. a quark-hadron mixed phase. They found a significant softening of the EoS in the mixed phase as well as the formation of a second shock wave as a direct consequence of the quark-hadron phase transition. The secondary shock followed and finally merged with the Fe-core bounce shock, only milliseconds after its appearance. However, both studies were not able to predict any possible features in the neutrino signal emitted due to the lack of neutrino transport. Simulations of the QCD phase transition of very massive ($100 M_{\odot}$) progenitors have been reported recently by Nakazato et al. (2008a) and Nakazato et al. (2010a). They applied the quark bag model for the quark matter EoS with a large bag constant and hence a high critical density for the onset of deconfinement. The transition from hadronic matter to quark matter was modeled via an extended mixed phase applying the Gibbs conditions. They confirmed a significant softening of the EoS in the mixed phase due to the reduced adiabatic index. A characteristic neutrino signature was not found due to the immediate formation of a black hole during the phase transition. However, they observed a significant shortening of the post bounce accretion time until black hole formation, due to the softening of the EoS at conditions where quark matter was found to occur.

TABLE 1
LIST OF NEUTRINO REACTIONS CONSIDERED, WHERE $\nu = \{\nu_e, \bar{\nu}_e, \nu_{\mu/\tau}, \bar{\nu}_{\mu/\tau}\}$ AND $N = \{n, p\}$.

Label	Neutrino reaction	Reference
1	$e^- + p \rightleftharpoons n + \nu_e$	Bruenn (1985)
2	$e^+ + n \rightleftharpoons p + \bar{\nu}_e$	Bruenn (1985)
3	$e^- + \langle A, Z \rangle \rightleftharpoons \langle A, Z - 1 \rangle + \nu_e$	Bruenn (1985)
4	$\nu + N \rightleftharpoons \nu' + N$	Bruenn (1985), Mezzacappa & Bruenn (1993b)
5	$\nu + \langle A, Z \rangle \rightleftharpoons \nu' + \langle A, Z \rangle$	Bruenn (1985), Mezzacappa & Bruenn (1993a)
6	$\nu + e^\pm \rightleftharpoons \nu' + e^\pm$	Bruenn (1985), Mezzacappa & Bruenn (1993c)
7	$e^- + e^+ \rightleftharpoons \nu + \bar{\nu}$	Bruenn (1985), Mezzacappa & Messer (1999)
8	$N + N \rightleftharpoons N + N + \nu + \bar{\nu}$	Thompson & Burrows (2001)
9	$\nu_e + \bar{\nu}_e \rightleftharpoons \nu_{\mu/\tau} + \bar{\nu}_{\mu/\tau}$	Buras et al. (2003), Fischer et al. (2009)

The present article follows a different approach. It is the continuation of Sagert et al. (2009), where first results were discussed. We construct a quark-hadron hybrid EoS, i.e. using the microscopic EoS from Shen et al. (1998) for hadrons and the bag model based EoS for strange quark matter. The resulting EoS is applied to core-collapse supernova simulations of low and intermediate mass Fe-core progenitors. Our model is based on general relativistic radiation hydrodynamics and three flavor Boltzmann neutrino transport in spherical symmetry. For these progenitors, spherically symmetric simulations do not result in explosions via the delayed neutrino heating mechanism (see e.g. Rampp & Janka 2000; Liebendörfer et al. 2001b; Janka 2001; Thompson et al. 2003). Here, we explore the possibility that a quark-hadron phase transition during the early post bounce evolution can result in an explosion and discuss the observational consequences. The temperatures on the order of tens of MeV and the large neutron excess of matter in supernova interiors, enables a phase transition at low critical densities close to nuclear saturation density (depending on the bag model parameters). In this respect, the physical conditions in core-collapse supernova interiors differ from matter in heavy-ion collision experiments, where temperatures on the order of few 100 MeV are obtained but matter stays more or less isospin symmetric with an electron fraction of $Y_e \simeq 0.5$. The expected critical density is on the order of several times nuclear saturation density in heavy-ion collision experiments. Furthermore, the supernova timescales (1–100 ms) and the timescale in heavy-ion collisions ($\sim 10^{-23}$ seconds) are substantially different. These differences will be further discussed in §2. In the core-collapse supernova simulations under investigation, the phase transition takes place within the first 500 ms post bounce (depending on the critical conditions and the progenitor model). We observe an accelerated PNS contraction due to the softening of the EoS in the mixed phase, in comparison to simulations using purely hadronic EoSs. The contraction proceeds into an adiabatic collapse when the maximum stable mass, depending on the hybrid EoS, is reached. During the collapse, density and temperature increase and a pure quark phase develops where the EoS is significantly stiffer than the EoS in the mixed phase. The collapse halts and a strong second shock front forms. This shock wave accelerates at the PNS surface where the density drops over several orders of magnitude, resulting in explosions with matter at outflow velocities on the order of 10^5 km/s. Furthermore, the shock propagation across the neutrinospheres which are located in the hadronic

phase, releases an additional neutrino burst dominated by $\bar{\nu}_e$ and $(\nu_{\mu/\tau}, \bar{\nu}_{\mu/\tau})$. We analyze the emitted neutrino signal from this explosion scenario for several examples of massive progenitors. The possible detection of the QCD induced neutrino burst has been investigated by Dasgupta et al. (2010) for a Galactic event, based on results from Sagert et al. (2009).

The manuscript is organized as follows. In § 2 we briefly discuss our core-collapse supernova model including the standard hadronic EoS. Furthermore, we explain the construction of the hybrid EoS in detail. We explore different choices of parameters and discuss the corresponding phase diagrams and hybrid star mass-radius relations. § 3 is devoted to the illustration of the results obtained for the $10.8 M_\odot$ progenitor from Woosley et al. (2002), that will be used as the reference model. The results are discussed in § 4, where we compare the reference model with simulations performed with different progenitor masses and different hybrid EoSs. Furthermore, we explore the nucleosynthesis relevant conditions and draw conclusions about the possibility of reaching high magnetic fields on the order of $10^{13} - 10^{15}$ G during the PNS evolution with quark matter. We close the manuscript with the summary in § 5.

2. NEUTRINO RADIATION HYDRODYNAMICS

The spherically symmetric radiation hydrodynamics model AGILE-BOLTZTRAN is based on three flavor Boltzmann neutrino transport. It solves the evolution of the neutrino distribution functions f_ν (phase-space functions) for each neutrino flavor $\nu = \{\nu_e, \bar{\nu}_e, \nu_{\mu/\tau}, \bar{\nu}_{\mu/\tau}\}$,

$$\frac{df_\nu}{dt} = \left. \frac{df_\nu}{dt} \right|_{\text{collision}} \quad (1)$$

depending on the phase-space derivative (l.h.s of Eq.(1)) and neutrino-matter interactions (r.h.s of Eq.(1)). The neutrino reactions for the various interactions considered are listed in Table 1, including the references. In spherical symmetry, the distribution functions depend on the phase-space coordinates system time t , baryon mass a , the cosine of the neutrino propagation angle $\mu = \cos\theta$ and the neutrino energy E , $f_\nu(t, a, \mu, E)$, where the latter two are the momentum space representations. The original Newtonian variant of AGILE-BOLTZTRAN (see Mezzacappa & Bruenn 1993a,b,c) has been extended by Liebendörfer et al. (2001a) to solve the general relativistic equations, based on non-stationary spacetime represented by the following line element

$$ds^2 = -\alpha(t, a)^2 dt^2 + \left(\frac{r(t, a)'}{\Gamma(t, a)} \right)^2 da^2 + r(t, a)^2 d\Omega,$$

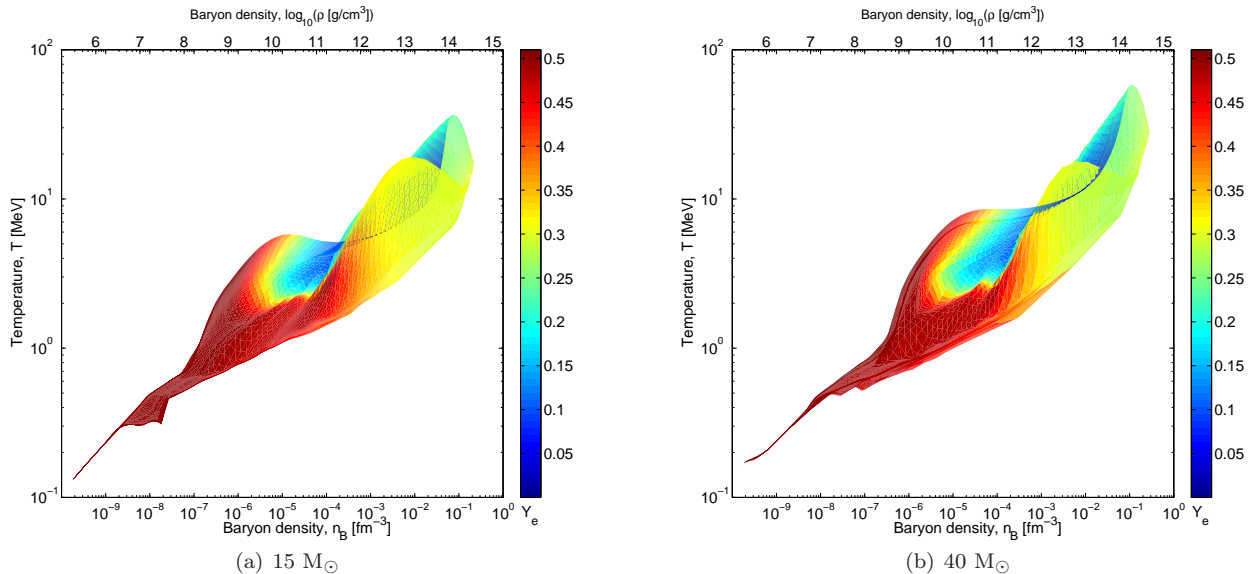


FIG. 1.— Phase space covered in core-collapse supernova simulations at the example of two progenitor models from Woosley & Weaver (1995), both using the pure hadronic EoS from Shen et al. (1998). The white background corresponds to densities and temperatures which are not obtained, where the colored domain belongs to densities and temperatures which are obtained. Color-scaled is the electron fraction which ranges from neutron matter (blue) $Y_e = 0$ to symmetric matter (red) $Y_e \simeq 0.5$.

where $d\Omega = d\theta^2 + \sin^2\theta d\phi^2$ is the line element of a 2-sphere of radius r in spherical coordinates (θ, ϕ) , and $r' = \partial r / \partial a$. Note that the metric functions α and Γ depend on the coordinates system time t and baryon mass a . The evolution equations for energy and momentum are obtained from the covariant derivative of the stress-energy tensor, $\nabla_i T^{ik} = 0$, with the following choice of the stress-energy tensor

$$T^{tt} = \rho(1 + e + J), \quad T^{aa} = p + \rho K, \quad T^{at} = T^{ta} = \rho H, \\ T^{\theta\theta} = T^{\phi\phi} = p + \frac{1}{2}\rho(J - K),$$

where ρ , p and e are the rest mass density, matter pressure and the internal energy density. J , H and K are the neutrino moments, which are given by the momentum integrals of the neutrino distribution functions (for details, see Liebendörfer et al. 2004). Special attention has been devoted to accurately conserve lepton number, energy and momentum, as described in details in Liebendörfer et al. (2004). General relativistic effects have been investigated with respect to the PNS collapse and black hole formation for several massive progenitor stars of 40 and 50 M_\odot in Fischer et al. (2009).

The numerical implementation of the above mentioned physical equations, including the finite differencing mass conserving scheme, has been introduced in Liebendörfer et al. (2002) and Liebendörfer et al. (2004), where recent improvements of the finite differencing scheme for the evolution of the enclosed baryon mass have been introduced in Fischer et al. (2010b). With these improvements, stable solutions for the evolution equations can be obtained for long simulation times on the order of seconds.

In the following subsections, we will introduce the EoS where the sophisticated baryon EoS from Shen et al. (1998) has been extended with a quark-hadron mixed and a pure quark phase at high densities and temperatures.

2.1. The EoS in core-collapse supernova simulations

The EoS has to handle a large variety of physical conditions obtained in core-collapse supernova simulations. The covered domain is illustrated in Fig. 1 for the examples of the 15 and 40 M_\odot progenitor models from Woosley & Weaver (1995) for the first second post bounce, both using the pure hadronic EoS from Shen et al. (1998). Temperatures and baryon densities reach from below 0.1 MeV and 10 g/cm^3 ($6 \times 10^{-15} \text{ fm}^{-3}$) up to 100 MeV and 10^{15} g/cm^3 (0.6 fm^{-3}). The electron fraction is represented on a color-scale, where low values of $Y_e \simeq 0.1$ are obtained close to the neutrinospheres at sub-saturation densities. For the low density domain, which is entirely given by the progenitor, matter is isospin symmetric with an electron fraction of $Y_e \simeq 0.5$. Furthermore, the figures show that only a narrow middle band of the (T, ρ) -diagram is covered in core-collapse supernova simulations of massive stars, e.g. low temperatures and high densities (which corresponds to neutron star matter) as well as vice versa are not obtained. This is because the entropy per baryon does not change over many orders of magnitude during the early (up to 1 second) post bounce evolution which is illustrated in Fig. 1.

2.1.1. Hadronic matter

For temperatures roughly below 0.5 MeV, the rates for nuclear reactions are important and the assumption of nuclear statistical equilibrium (NSE) cannot be applied. The baryon contributions to the EoS are given by nuclear abundances which must be evolved in time. The dynamical evolution of these abundances are calculated using the nuclear reaction network developed by Thielemann et al. (2004) (and references therein) which employs tabulated reaction rates. Due to current computational limitations, we employ the free nucleons, and in addition ${}^3\text{He}$ and ${}^4\text{He}$ as well as the 13 symmetric nuclei starting from ${}^{12}\text{C}$ to ${}^{56}\text{Ni}$. Furthermore, we use the following 3 asymmetric nuclei ${}^{53}\text{Fe}$, ${}^{54}\text{Fe}$ and ${}^{56}\text{Fe}$. The details of the implemen-

tation of the network into AGILE-BOLTZTRAN as well as the motivation for our choice of nuclei and the use in core-collapse supernova models, is given in Fischer et al. (2010b). It is of special importance to mimic the energy generation from nuclear burning processes in explosion models, where the explosion shock travels through the low temperature and density envelop of the progenitor and the simplification of the ideal gas of Si-nuclei cannot be used.

For higher temperatures, matter is assumed to be in NSE and the production and destruction of nuclei are in thermal and chemical equilibrium with respect to strong interactions. The abundances depend only on the thermodynamic state given by the temperature T , the baryon density ρ (alternatively n_B) and the electron fraction Y_e . For this regime, we use the hadronic EoS from Shen et al. (1998). It is based on the relativistic mean field (RMF) approach for homogeneous matter and the Thomas-Fermi-approximation for a single average heavy nucleus. It has an incompressibility modulus of 281 MeV and an asymmetry energy of 36.9 MeV. For this stiff EoS, cold neutron stars with maximum mass of 2.2 M_\odot are obtained (see the black solid line in Fig. 7(a)).

On top of the baryons, contributions from electrons and positrons as well as photons and coulomb corrections (only for non-NSE) are added, based on Timmes & Arnett (1999).

2.1.2. Quark matter in the bag model

Bag models are phenomenological models which were originally introduced to describe quark confinement. Due to their simple handling and ability to reproduce hadron properties (see e.g. Chodos et al. 1974b; Degrand et al. 1975; Detar & Donoghue 1983), they are also often applied for bulk quark matter and phase transitions in compact star interiors. The first description of a bag model goes back to Bogolyubov (1968) and was improved a few years later by Chodos et al. (1974b), known today as the MIT bag model. The main idea of quark bag models is that the true vacuum of QCD is a medium which refuses the penetration of quarks and confines them within a sphere (or a bag) to form a color neutral hadron. The QCD vacuum exerts a pressure on the hadron, represented phenomenologically by the bag constant B , which is opposed by the motion of the interior quarks. Within the bag, quarks are assumed to move in asymptotic freedom with vanishing or current masses. Their total pressure p^Q , energy density ϵ^Q , entropy density s^Q , and baryon number density n_B^Q can be written as follows

$$p^Q = \sum_i p_i - B, \quad \epsilon^Q = \sum_i \epsilon_i + B, \quad (2)$$

$$s^Q = \sum_i s_i, \quad n_B^Q = \frac{1}{3} \sum_i n_i, \quad (3)$$

where the sums run over all present quark flavors i . In the simple bag model quarks are treated as non-interacting fermions and their contributions in the above sums can be calculated by solving the corresponding Fermi integrals for given temperature T , quark chemical potential

μ_i , and mass m_i as follows

$$p_i(m_i, T, \mu_i) = \frac{1}{3} \frac{g_i}{2\pi^2} \int_0^\infty k^2 dk k \frac{\partial E_i(k)}{\partial k} \times [f(k, \mu_i) + f(k, -\mu_i)] \quad (4)$$

$$\epsilon_i(m_i, T, \mu_i) = \frac{g_i}{2\pi^2} \int_0^\infty E_i(k) k^2 dk \times [f(k, \mu_i) + f(k, -\mu_i)] \quad (5)$$

$$s_i(m_i, T, \mu_i) = \frac{g_i}{2\pi^2} \int_0^\infty k^2 dk [-f(k, \mu_i) \ln f(k, \mu_i) - (1 - f(k, \mu_i)) \ln(1 - f(k, \mu_i)) - f(k, -\mu_i) \ln f(k, -\mu_i) - (1 - f(k, -\mu_i)) \ln(1 - f(k, -\mu_i))] \quad (6)$$

$$n_i(m_i, T, \mu_i) = \frac{g_i}{2\pi^2} \int_0^\infty k^2 dk \times [f(k, \mu_i) - f(k, -\mu_i)]. \quad (7)$$

$f(k, \pm\mu_i)$ are the Fermi distribution functions with chemical potentials for particles ($+\mu_i$) and antiparticles ($-\mu_i$),

$$f(k, \pm\mu_i) = \frac{1}{e^{(E_i(k) \mp \mu_i)/T} + 1}, \quad (8)$$

where k is the momentum and $E_i(k) = \sqrt{m_i^2 + k^2}$ is the quark Fermi energy. The number of degrees of freedom for each flavor g_i consists of 2 spin states and 3 colors.

Various approaches have been introduced to extend and improve the simple bag model (see e.g. Detar & Donoghue 1983), including first order corrections for the strong coupling constant α_s (see e.g. Farhi & Jaffe 1984). Since analytical expressions for the thermodynamic potentials at finite temperature and including α_s corrections can only be obtained for massless quarks, we calculate the pressure of massive quarks for the flavor i as follows

$$p_i(m_i, T, \mu_i, \alpha_s) = p_i(m_i, T, \mu_i, 0) + [p_i(0, T, \mu_i, \alpha_s) - p_i(0, T, \mu_i, 0)] = p_i(m_i, T, \mu_i, 0) - \left[\frac{7}{60} T^4 \pi^2 \frac{50\alpha_s}{21\pi} + \frac{2\alpha_s}{\pi} \left(\frac{1}{2} T^2 \mu_i^2 + \frac{\mu_i^4}{4\pi^2} \right) \right]. \quad (9)$$

The last two terms in Eq.(9) are taken from analytical expressions in Farhi & Jaffe (1984), where $p_i(m_i, T, \mu_i, 0)$ can be calculated by numerically solving the Fermi integrals. The energy density ϵ_i , number density n_i , and entropy density s_i can be calculated in a similar way. We will apply this procedure only for the strange quarks, for which we choose a mass of $m_s = 100$ MeV in accordance with the range of $m_s \sim 70$ –130 MeV and the weighted average of $105_{-1.3}^{+1.5}$ MeV from Amsler (2008). The up and down quarks have masses of several MeV

and can be treated as massless, that is $m_u = m_d = 0$. The remaining quark flavors are too heavy to appear in supernova and neutron star environments.

The value of the bag constant is an active subject of research and expected to be in the range of $B^{1/4} \sim 145\text{--}235$ MeV, from hadron fitting (Detar & Donoghue 1983). An upper limit is difficult to define. However, concerning compact stars a value of $B^{1/4} \lesssim 200$ MeV allows the presence of a small pure quark matter core in the star interior (see e.g. Schertler et al. 2000). The lower limit for the bag constant depends on whether strange quark matter is considered as the ground state of nuclear matter or not. This absolute stability was introduced by Witten (1984) and is based on the idea that hadronic matter is a metastable state while strange quark matter has a lower energy per baryon than ^{56}Fe and is therefore the true ground state of nuclear matter. This so-called *Witten hypothesis* leads to the existence of strange stars, which are composed of absolutely stable strange quark matter. These can either represent all compact stars or be in co-existence with hadronic stars, as was recently discussed by Bauswein et al. (2009).

In the simple bag model with $m_u = m_d = 0$ and $m_s = 100$ MeV, the absolute stability of strange quark matter sets in for $B^{1/4} \lesssim 161$ MeV. For finite α_s and different quark masses, Farhi & Jaffe (1984) have mapped out the limiting values of B (see also Weissenborn et al. 2011, for different α_s). In the present article, we will not assume that strange quark matter is absolutely stable. However, since our aim is to probe low critical densities for the quark matter phase transition in the early post-bounce phase of supernovae, we chose the parameter sets of $B^{1/4} = 162$ MeV (EOS1) and $B^{1/4} = 165$ MeV (EOS2) both with $\alpha_s = 0$ and $B^{1/4} = 155$ MeV with $\alpha_s = 0.3$ (EOS3).

2.2. The hybrid EoS

To probe the appearance of quark matter in supernova environments we implement the quark-hadron phase transition into the pure hadronic EoS from Shen et al. (1998). The critical density for the onset of quark matter and the properties of the mixed phase depend strongly on the choice of global or local conservation laws. In this work we will apply the Gibbs approach as discussed in Glendenning (1996), where conservation laws are always fulfilled globally and the pressure in the mixed phase is a smooth function of the density (see Figs. 2(a) and 2(b)).

Another frequently used method to calculate phase transition is the Maxwell construction. Here only the baryon number is a global quantity and other conservation laws must be fulfilled locally in the quark and hadronic phases. As a consequence of this restriction, the onset of the mixed phase for the Maxwell condition is generally later (i.e. at higher density). Furthermore, for an isothermal phase transition the pressure is constant throughout the entire mixed phase, with respect to the baryon density.

Despite their different behaviors, the Maxwell and the Gibbs approaches both represent first order phase transitions. Gibbs falls in the class of non-congruent phase transitions whereas the restriction to only one globally conserved quantity in the case of a Maxwell construction is congruent (for details on (non)congruent phase

transitions, see e.g. Iosilevskiy 2010). Similar to the pasta phases in nuclear matter at the liquid-gas phase transition, finite size effects from e.g. Coulomb interactions and surface tension of quark or hadronic matter can lead to the formation of structures in the mixed phase, like spheres, rods, and planes. It was shown by e.g. Yasutake et al. (2009), that such a scenario can make the quark-hadron phase transition very similar to the one given by a Maxwell construction. However, in the present article we neglect any finite-size effects and Coulomb contributions and treat the phases in the thermodynamic limit.

Both the Maxwell and the Gibbs approaches are used in astrophysics and nuclear physics frequently. However, they represent only two extreme scenarios for equilibrium conditions at the phase transition. It was recently shown by Hempel et al. (2009) that the actual variety of possible combinations of global and local conservation laws is much richer and can open up interesting new scenarios for e.g. the early evolution of protoneutron stars (Pagliara et al. 2009).

Chemical potentials which correspond to a globally conserved quantity k , are equal in the quark and hadron phases. Together with thermal and mechanical equilibrium of quark and hadronic matter, the conditions for the co-existence region are:

$$T^H \equiv T^Q \quad (10)$$

$$\mu_k^Q \equiv \mu_k^H \quad (11)$$

$$p^H \equiv p^Q. \quad (12)$$

The pressures p^H and p^Q , in the hadronic and quark phases, respectively, are in principle sums over contributions from all present particles, including electrons and neutrinos. As discussed in §2.1, the high temperatures and densities when quark matter sets in, correspond to conditions where neutrinos are completely trapped. Hence, neutrinos are in weak equilibrium with nuclear matter at given lepton fraction Y_L (see e.g. Steiner et al. 2000; Pagliara et al. 2009), together with the electrons and positrons. However, within the Gibbs approach the electron and neutrino chemical potentials are equal in the quark and hadronic phases and so are their contributions to the thermodynamic quantities such as the pressure, which consequently cancel in the equilibrium condition of Eq.(12). In this context, it was recently discussed by Hempel et al. (2009) that neutrino contributions do not in fact have to be taken into account, neither for the Gibbs nor the Maxwell construction if the EoS is provided for given temperature T , baryon density n_B and proton fraction Y_p .

The chemical potentials for the up and down quarks can be obtained from the equilibrium conditions at deconfinement as follows

$$p \rightleftharpoons 2u + d, \quad n \rightleftharpoons 2d + u, \quad (13)$$

where

$$\mu_u = \frac{2}{3}\mu_p - \frac{1}{3}\mu_n, \quad \mu_d = \frac{2}{3}\mu_n - \frac{1}{3}\mu_p. \quad (14)$$

The dynamical timescales considered in supernova simulations can be as small as milliseconds. On the other hand, weak reactions producing strangeness oper-

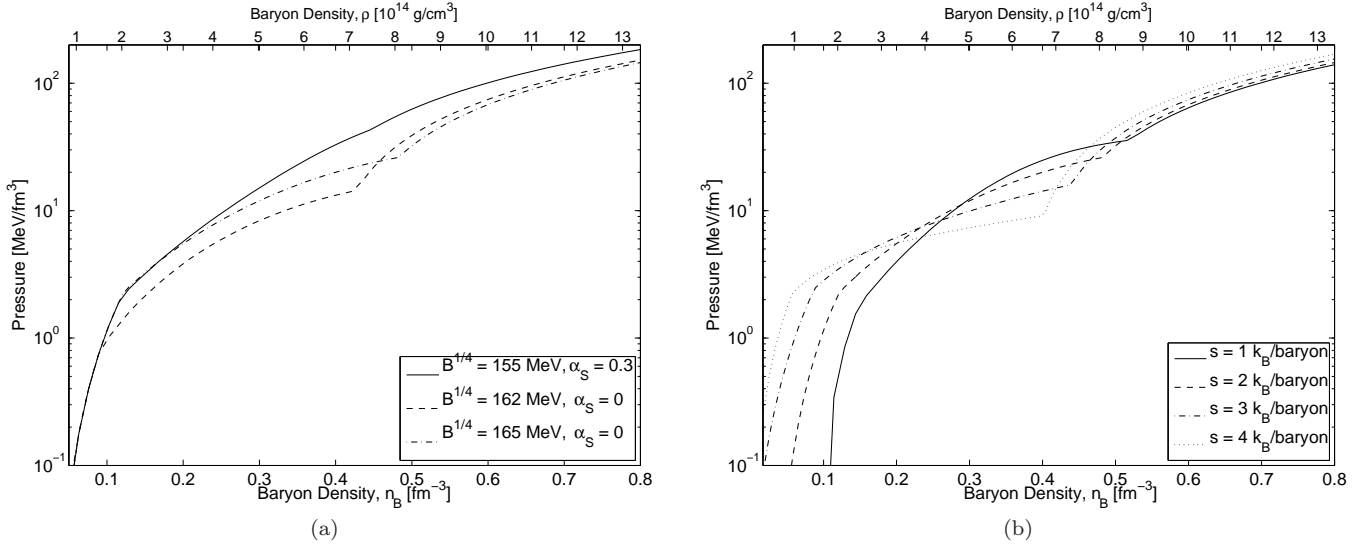


FIG. 2.— Hybrid EoS with a global proton fraction of $Y_p = 0.3$. (a) shows the pressure versus density for fixed entropy per baryon of $s = 2 k_B$, for different bag constants B and α_s . (b) shows pressure versus density for different entropies per baryon at fixed bag constant of $B^{1/4} = 165$ MeV and $\alpha_s = 0$. Due to the smaller critical density, the EoS in the co-existence region is softer for higher values of s .

ate much faster on the order of 10^{-6} s (from kaon decays; Amsler 2008). The latter should be equilibrated in nuclear matter and hence be present either already in the hadronic phase in form of hyperons (see e.g. Ishizuka et al. 2008) or be produced by a series of weak reactions in the quark phase, that can be schematically expressed by the following effective reaction



which leads to $\mu_s = \mu_d$ for the strange quark chemical potential. Consequently, we consider quark matter composed of the three flavors up, down, and strange. We did not implement hyperons or kaons in the hadronic phase, because our main goal is to study the effects from quark matter in core-collapse supernovae. However, such inclusion of strange hadrons, also in connection with strangeness conserving quark matter phase transitions, is of high interest and should be addressed in future studies.

The mixed phase is characterized by the fraction of quark matter χ , as follows

$$\chi = \frac{V^Q}{V^Q + V^H}, \quad (16)$$

where V^Q and V^H are the volume fractions of the quark and hadronic phases, respectively. Consequently,

$$\begin{aligned} \chi &= 0 && \text{(hadronic phase),} \\ 0 < \chi < 1 && \text{(mixed phase),} \\ \chi &= 1 && \text{(quark phase).} \end{aligned}$$

For $0 < \chi < 1$, the baryon number density n_B , the energy density ϵ , and the entropy density s are calculated as a sum of the quark and the hadron contributions via the following expressions

$$n_B = (1 - \chi)n_B^H + \chi n_B^Q, \quad (17)$$

$$\epsilon = (1 - \chi)\epsilon^H + \chi\epsilon^Q, \quad (18)$$

$$s = (1 - \chi)s^H + \chi s^Q. \quad (19)$$

Furthermore, within the Gibbs approach, the proton fraction Y_p is a global quantity and composed of the charge fractions in the hadronic and the quark phases as follows

$$Y_p n_B = (1 - \chi)Y_c^H n_B^H + \chi Y_c^Q n_B^Q, \quad (20)$$

where $Y_c^H = n_p/n_B^H$ (hadronic matter) and $Y_c^Q = n_c^Q/n_B^Q$ (quark matter) are calculated from the positively charged up and negatively charged down and strange quarks via $n_c^Q = (2n_u - n_d - n_s)/3$.

2.3. Discussion of the Hybrid EoS

Fig. 2(a) shows the pressure with respect to the baryon density for different values of B and α_S as well as for different entropies per baryon. The EoSs are calculated for a global proton fraction of $Y_p = 0.3$ at fixed entropy $s = 2 k_B$ /baryon. The onset of the mixed phase happens for all parameter sets around nuclear saturation density. It can be identified by a softening of the EoS¹, while the appearance of the pure quark matter phase is accompanied by a stiffening. In the following, we will discuss the origin of these changes in the pressure slopes while their effects on the supernova dynamics will be addressed in §3.

For the simple bag model, without α_s corrections, the smaller bag constant $B^{1/4} = 162$ MeV leads to an earlier onset of the mixed phase and therefore also to a lower pressure in the co-existence region than for $B^{1/4} = 165$ MeV. However, as given in Eq.(2) and can be seen from Fig. 2(a), for pure quark matter the larger bag constant gives a lower total pressure, while the inclusion of first order α_s corrections stiffens the quark EoS (see also Alford et al. 2005). Hereby, the accompanying shift in the critical density to higher values can be decreased again by lowering the bag constant (in our case $B^{1/4} = 155$ MeV) (see Sagert et al. 2010). However, the

¹ The softness/stiffness of the EoS is measured via the adiabatic index $\gamma = \partial \ln p / \partial \ln \rho$.

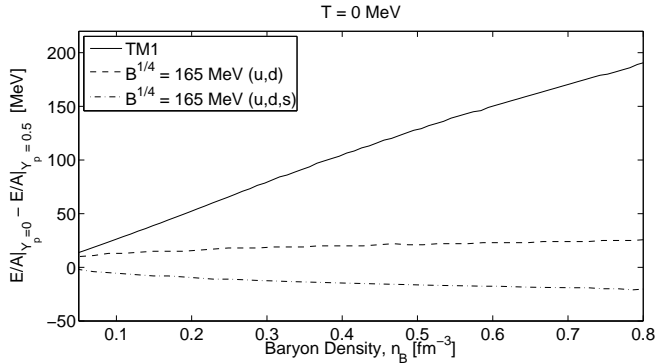


FIG. 3.— Symmetry energy of hadronic matter from Shen et al. (1998) (solid line), 2 flavor quark matter (dashed line) and three flavor quark matter (dash-dotted line) within the quark bag model with $B^{1/4} = 165$ MeV.

higher pressures in the mixed and the quark phases due to α_s corrections remain. With increasing entropy, the critical density shifts to lower values, and furthermore the pressure in the mixed phase is reduced (see Fig. 2(b)).

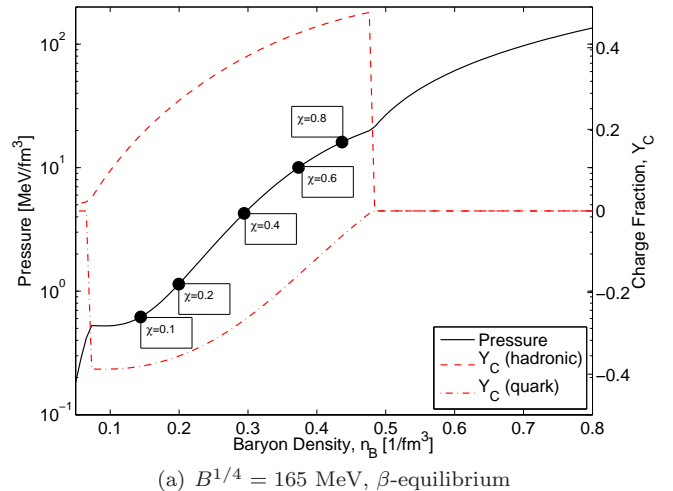
The global proton fraction Y_p also impacts the critical density due to the symmetry energy E_{sym} of hadronic and quark matter. For nucleons, E_{sym} is composed of a potential part which is caused by isospin dependent nucleon-nucleon interactions and a kinetic part stemming from the proton and neutron Fermi energies. In contrast, quark matter in the bag model is sensitive to its isospin state only by the Fermi energies of the quarks and has therefore a smaller symmetry energy than hadronic matter. This can be seen in Fig. 3, which shows E_{sym} for hadronic matter, for two-flavor and for three-flavor quark matter with $B^{1/4} = 165$ MeV (see also Pagliara & Schaffner-Bielich (2010)). The symmetry energy can be defined by the difference of the energy per baryon of pure neutron matter, that is $Y_p = 0$, and isospin symmetric matter with $Y_p = 0.5$ (see Li et al. 2008)

$$E_{sym}(n_B) \propto \frac{E}{A} \Big|_{n_B, Y_p=0} - \frac{E}{A} \Big|_{n_B, Y_p=0.5}. \quad (21)$$

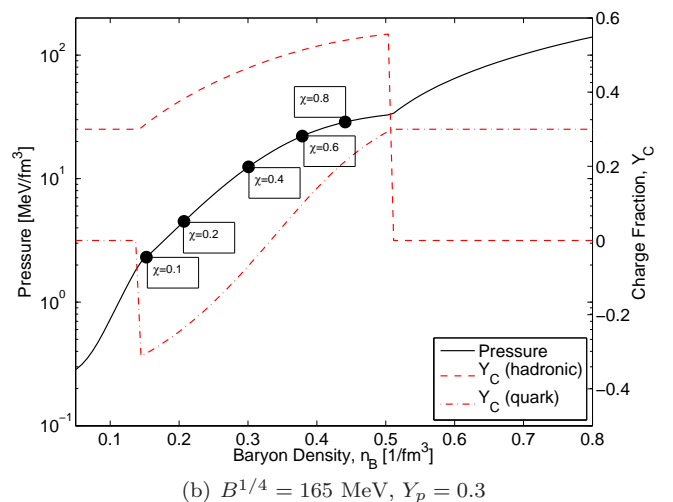
Because the down and strange quarks have negative charge, they can replace the electrons as agents for charge neutrality. In Fig. 3, β -equilibrium² was assumed, which leads to compositions with small values of Y_c or Y_c^Q , respectively. As a consequence, we see in Fig. 3 that E_{sym} is even negative for strange quark matter in contrast to two flavor quark matter and hadronic matter.

In Fig. 4(a), the charge fractions Y_c^H and Y_c^Q are plotted as functions of the baryon density for the mixed phase as well as the regions with pure hadronic and quark matter. The quark EoS is calculated using $B^{1/4} = 165$ MeV in β -equilibrium at $T = 0$. As described by Glendenning (1996), the large asymmetry energy in hadronic matter can be relieved by arranging the up, down, and strange quark fractions in the mixed phase to negative values of Y_c^Q . This is also mirrored in the behavior of the EoS which experiences a prompt softening at the beginning of the mixed phase, seen in Fig. 4(a). With growing amount of quarks and decreasing contribution

² β -equilibrium is given by the following relation between the chemical potentials $\mu_e + \mu_p = \mu_n$ (see e.g. Weber 1999)



(a) $B^{1/4} = 165$ MeV, β -equilibrium



(b) $B^{1/4} = 165$ MeV, $Y_p = 0.3$

FIG. 4.— Pressure (black solid lines) and charge fractions in the hadronic and quark phase, Y_c^Q (red dash-dotted lines) and Y_c^H (red dashed lines), respectively, for matter in β -equilibrium in graph (a) and at a fixed global proton fraction of $Y_p = 0.3$ in graph (b). Both calculations are done for zero temperature and show the corresponding pressure-density curves, together with different quark volume fractions χ in the mixed phase.

from hadronic matter, the latter can approach its energetically more favorable state with $Y_c^H \sim 0.5$, while the charge fraction in the quark phase reaches the discussed small value of $Y_c^Q \sim 0$.

As shown in Fig. 4(b), for $Y_p = 0.3$ the EoS does not experience a significant softening at the onset of the phase transition, but stays similar to the one of pure hadronic matter. The reason is that at $Y_p = 0.3$ nucleonic matter is already close to its energetically favorable isospin symmetric state. Only for larger χ the lower pressure of quark matter starts to dominate and the EoS in the mixed phase softens.

Due to the dependence of the hadronic EoS on Y_p , the critical density for the phase transition is also sensitive to the proton fraction. The earlier onset of the mixed phase for smaller values of Y_p was already presented by Drago & Tambini (1999) and is seen in the Figs. 5(a), 5(b) and 5(c) for $B^{1/4} = 165$ MeV, $B^{1/4} = 162$ MeV and $B^{1/4} = 155$ MeV with $\alpha_s = 0.3$, respectively (see also

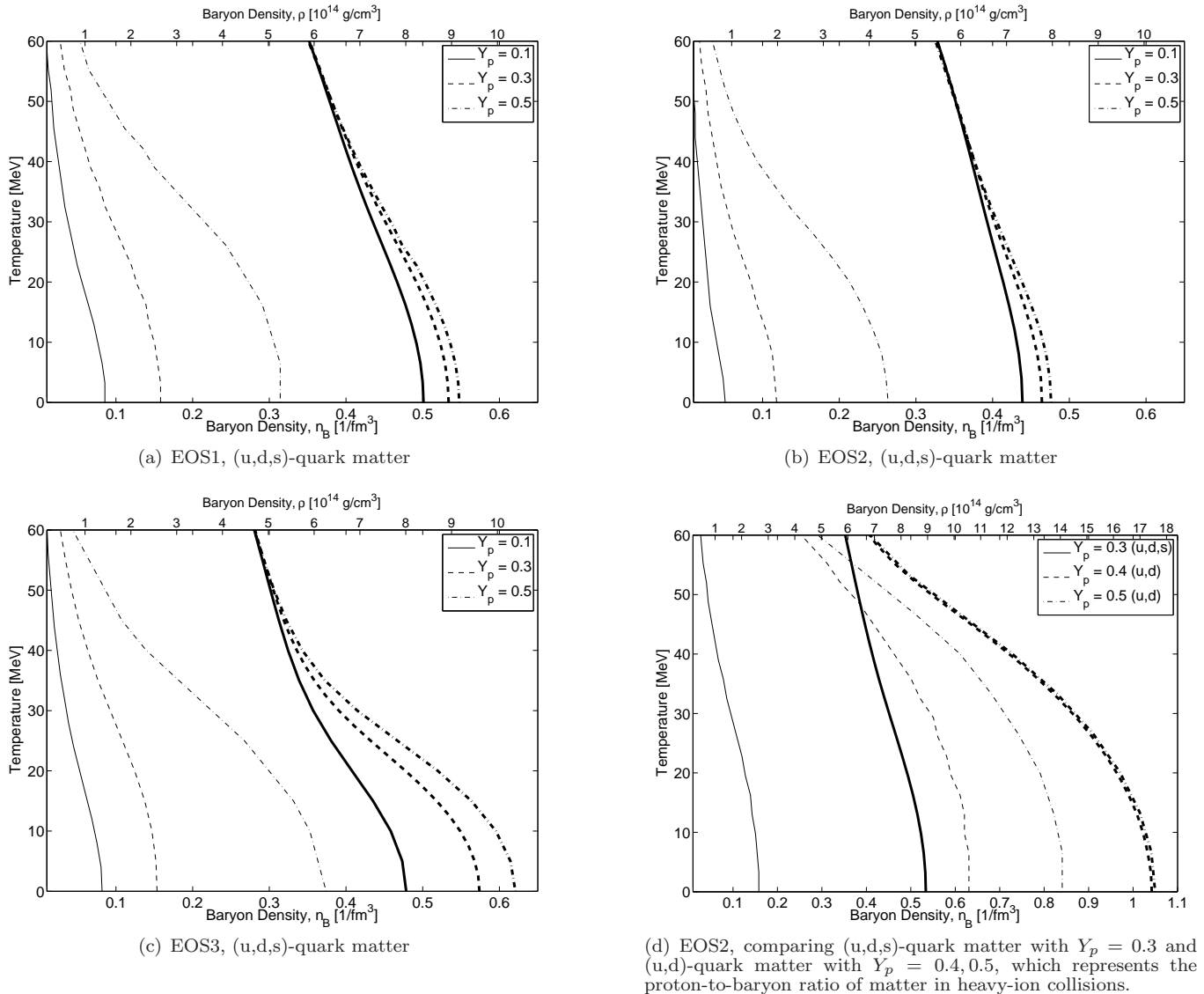


FIG. 5.— Phase diagrams for transitions from hadronic matter based on Shen et al. (1998) (RMF, TM1) to strange quark matter with fixed local proton fractions of $Y_p = 0.1, 0.3$, and 0.5 and different quark EoS parameter choices in the graphs (a)-(c). In addition, Fig. (d) compares a phase diagram for the conditions in supernova environments where $Y_p = 0.3$ (strange quark matter) with heavy-ion collisions where the proton fraction is close to isospin symmetry and the phase transition takes place from hadronic to up and down quark matter. The thin lines show the onset of quark matter and the thick lines the pure quark phase.

Fischer et al. 2010a).

Another important aspect for the phase transition is the different number of degrees of freedom of hadronic and quark matter. As discussed above, it is appropriate to assume the quark-hadron phase transition to strange quark matter in supernovae. The strange quarks are produced and equilibrated by weak interactions in supernova environments due to the timescales which are on the order of milliseconds. In heavy-ion collisions, the hot fireball of nuclear matter expands within 10^{-23} seconds (Kolb et al. 2000) and thereby prevents the appearance of net strangeness via weak reactions. Hence, the quark-hadron phase transition occurs only to up- and down-quark matter in heavy-ion collision experiments. Furthermore, for supernovae and neutron stars we can regard phase transitions from hadronic matter to strange quark matter at low global proton fractions $Y_p \ll 0.5$. In heavy-ion collisions, the colliding nuclei are close to

isospin symmetry with a proton fraction of $Y_p \simeq 0.5$. In the case of only two flavor quark matter, the stiffening of the quark EoS due to the fewer degrees of freedom and the softness of hadronic matter makes a phase transition to quark matter less favorable and shifts the critical density to higher values. As shown in Fig. 5(d), a low critical density close to normal nuclear matter density in supernova and neutron star environments is compatible with a high critical density (five times nuclear matter density) in heavy ion experiments, based on the simple bag model for the description of quark matter.

The Figs. 6(a) - 6(d) show the evolution of the temperature in the pure and the mixed phases along different isentropes (i.e. curves of constant entropy per baryon) for fixed proton fraction and three-flavor quark matter. Hereby, the Figs. 6(a) - 6(c) give the phase diagrams for $B^{1/4} = 165$ MeV for different values of Y_p

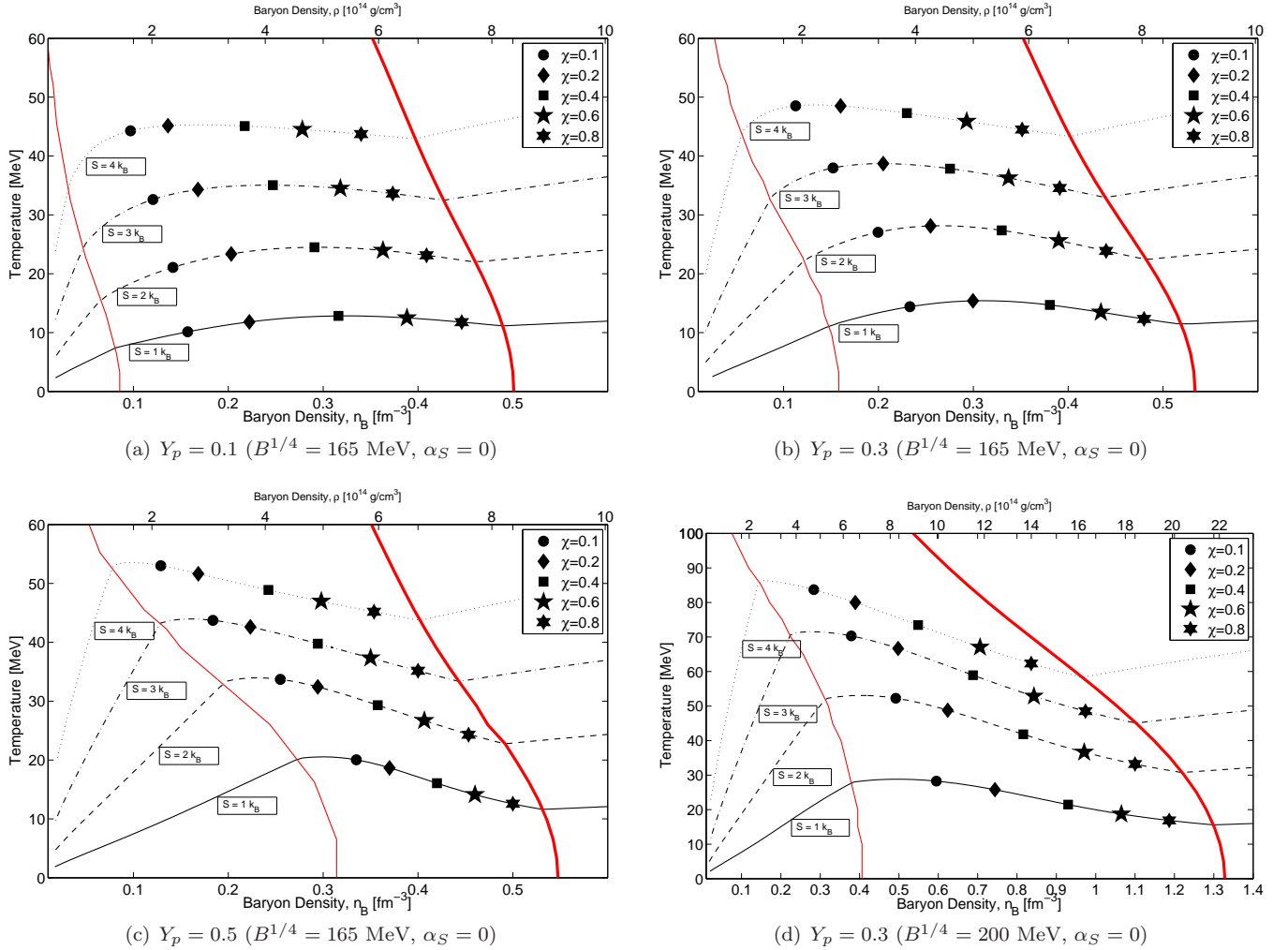
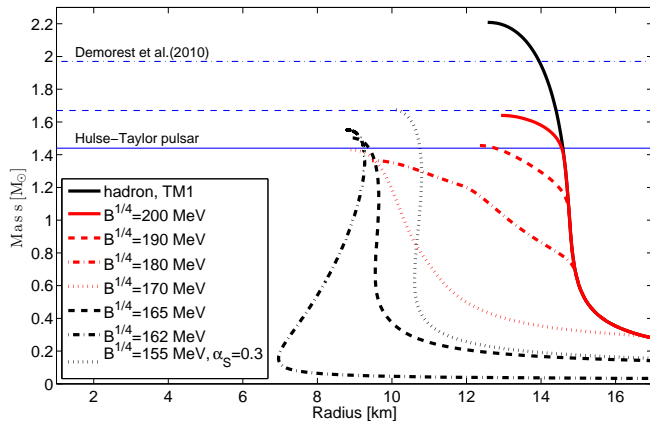


FIG. 6.— Temperature evolution in the mixed phase for the different entropies per baryon $s = 1, 2, 3, 4 k_B$. The graphs (a) - (c) show calculations for global proton fractions of $Y_p = 0.1$, $Y_p = 0.3$ and $Y_p = 0.5$ with $B^{1/4} = 165$ MeV. The red solid lines show the onset of the mixed phase (thin lines) and the beginning of the pure quark phase (thick lines) and are the same as in Fig. 5(a). For comparison, the graph (d) shows the temperature evolution in the mixed phase for $Y_p = 0.3$ and $B^{1/4} = 200$ MeV.

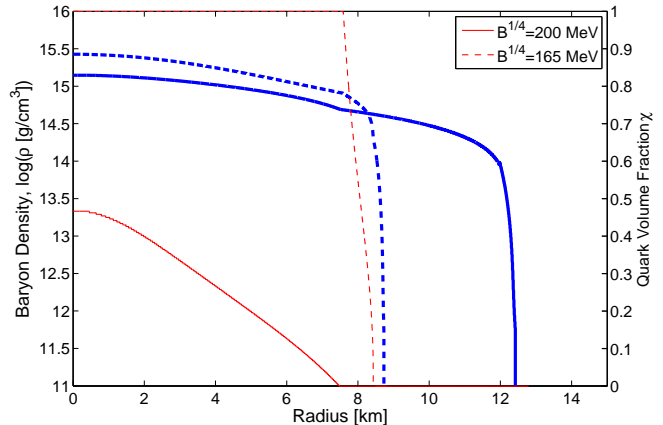
while the Fig. 6(d) shows the temperature evolution for $B^{1/4} = 200$ MeV and $Y_p = 0.3$. Steiner et al. (2000) and Nakazato et al. (2010b) discuss such a temperature evolution along isentropes for $B^{1/4} \sim 200$ MeV at a fixed lepton fraction Y_L . The authors find a temperature decrease in the mixed phase due to the larger number of degrees of freedom and the different heat capacity for relativistic quarks.

However, Drago & Tambini (1999) showed that the behavior of T in the mixed phase depends on the critical density and the temperature at the onset and at the end point of the mixed phase, which is set by Y_p . The temperature behavior based on the quark bag model can be seen from the Figs. 6(a) and 6(b) in comparison to 6(c) and 6(d). For early phase transitions, the temperature curves rise in the beginning of the mixed phase, while for high critical densities the temperature in the hadronic phase has already reached large values and the onset of quark matter causes a prompt temperature decrease along the isentropes. These results are in qualitative agreement with the previous studies of Steiner et al. (2000) and Nakazato et al. (2010b).

Dynamical simulations (e.g. in astrophysics and heavy-ion collisions) that use microscopic EoSs raise the question about convexity, in particular if phase transitions are included. In the context of phase transitions, one very often discusses the convexity of the thermodynamic potential (in our case the Helmholtz free-energy, see e.g., Müller & Serot 1995): If the thermodynamic potential is a convex function of its arguments, the system is thermodynamically stable. Due to the construction of the quark-hadron mixed phase and the stability of each phase separately, our hybrid EoS is stable and thus convex. However, another definition of convexity can be found in the literature in the context of the hydrodynamic Riemann problem, which refers to the curvature of the pressure as a function of density along isentropes. This property of the EoS is particularly relevant for shock waves traversing the coexistence region of a first order phase transition (see e.g. Rischke et al. 1990; Bugaev et al. 1989) as unusual wave patterns and effects like wave splitting can occur. Within this definition of convexity, Heuze et al. (2008) explored whether finite volume methods give a reasonable description of



(a) Mass-radius relations for the hadronic star using the EoS from Shen et al. (1998) (TM1,RMF) and hybrid stars with different bag constants using the Gibbs construction for the phase transition. The horizontal lines show three different observational constraints.



(b) Neutron star density profiles (thick blue lines) including the quark volume fractions (thin red lines).

FIG. 7.— Different mass-radius relations, comparing different bag constants, in graph (a) and neutron star density profiles, for two selected bag constants, in graph (b). The stiffening of the hybrid EoS when corrections from the strong coupling constant α_S are included, leads to higher maximum masses of the hybrid star branches. Small values of $B^{1/4} \lesssim 170$ MeV as well as large bag constants of $B^{1/4} > 190$ MeV can reach the mass limit of $1.44 M_\odot$ (horizontal solid line in graph (a)). Additionally, mass limits of $1.65 M_\odot$ (PSR J1903+0327, Freire & Wex 2010, horizontal dashed line) and $1.97 \pm 0.04 M_\odot$ (PSR J1614-2230, Demorest et al. 2010, horizontal dash-dotted line) are also shown in graph (a). The pure quark phase in the maximum mass configuration is large for small bag constants, while for $B^{1/4} = 200$ MeV quark matter is present only in form of a mixed phase.

a Riemann problem with a non-convex EoS. After performing such a test we can conclude that AGILE belongs to the class of hydrodynamics codes, which show a satisfactory agreement with the analytical solutions.

2.4. Masses and Radii of Hybrid Stars

Fig. 7(a) shows hybrid star mass-radius relations for the hadron EoS from Shen et al. (1998) and the bag model for different values of B and α_S . For comparison, we indicate the mass of the Hulse-Taylor pulsar of $M \sim 1.44 M_\odot$ ³. For simple quark bag models where the phase transition is constructed applying the Gibbs conditions, only the small values of $B^{1/4} \lesssim 170$ MeV as well as large bag constants of $B^{1/4} > 190$ MeV can reach this limit. However, as shown in Fig. 7(b), hybrid stars constructed using $B^{1/4} = 200$ MeV, do not contain pure quark matter but only the mixed phase with quark matter fractions of $\chi \lesssim 0.5$. In contrast, for the small bag constant $B^{1/4} = 165$ MeV the hybrid star at maximum mass is almost completely composed of pure quark matter, with only a thin hadronic crust with a thickness of up to one kilometer. As will be discussed in the following, the small value of the critical density and the resulting early phase transition to quark matter, together with the stiffening of the EoS in pure quark matter, lead to very specific dynamical consequences for the core-collapse supernova which may not be reached for large values of B due to the high critical density and absence of the stiffening of the hybrid EoS.

Recent mass limits for physical EoSs come from the millisecond pulsars J1903+0327 and J1614-2230 which were announced to have masses of $M = 1.67 \pm 0.01 M_\odot$ (Freire & Wex 2010) and $M = 1.97 \pm 0.04 M_\odot$

³ The Hulse-Taylor pulsar is the highest precisely known mass of compact stars, at present. It represents therefore a minimal limit for masses which should be reachable with realistic nuclear EoSs.

(Demorest et al. 2010), respectively. As shown in Fig. 7(a), within the simple bag model such masses can only be reached for bag constants of $B^{1/4} > 200$ MeV. Further corrections from the strong interaction coupling constant can stiffen the normal bag EoS and therefore lead to higher maximum masses of compact stars (see e.g. Schertler et al. 2000; Alford et al. 2005; Sagert et al. 2010; Weissenborn et al. 2011). It can be seen from Fig. 7(a) that the chosen parameter set $B^{1/4} = 155$ MeV and $\alpha_S = 0.3$ gives a maximum mass of hybrid stars of $M_{\text{max}} \sim 1.67 M_\odot$, which would be compatible with the observation of J1903+0327 (Freire & Wex 2010). The recent mass measurement by Demorest et al. (2010) points to an even higher neutron star mass of $1.97 \pm 0.04 M_\odot$. However, as discussed in e.g. Kurkela et al. (2010); Alford et al. (2005, 2007); Ozel et al. (2010), such high values exclude neither the presence of quark matter in compact star interiors nor low critical densities. The stiffening effect of strong interactions on the quark EoS can be modeled in our approach by e.g. according choices of larger values of α_S and will be tested in the future.

2.5. Neutrino interaction treatment in quark matter

Based on the parameters chosen for the bag model as discussed in the previous subsections, quark matter occurs at nuclear matter densities. At such high densities, the neutrino mean free paths are extremely small and neutrinos are trapped. Hence, we always assume chemical, weak and thermal equilibrium when determining the neutrino chemical potentials in quark matter.

3. SIMULATION RESULTS

In this section, we report on results from core-collapse supernova simulations in spherical symmetry where we apply the quark-hadron hybrid EoSs introduced in §2.3. The quark-hadron phase transition was found to occur during the early post bounce phase within the first

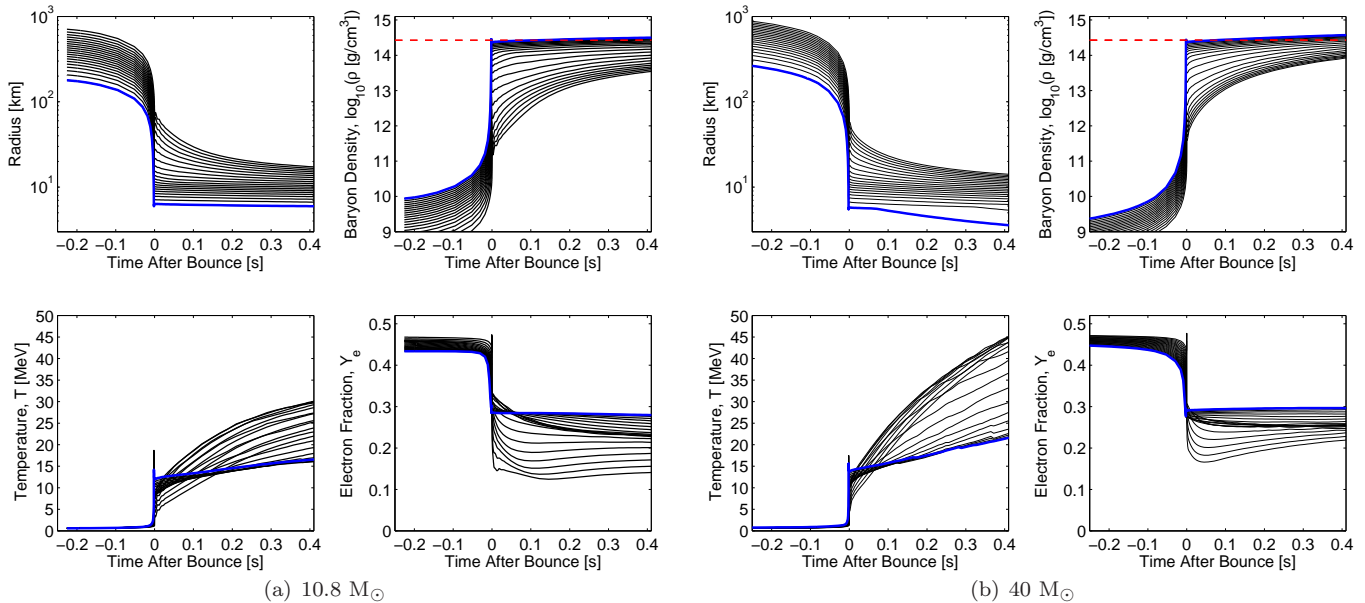


FIG. 8.— Evolution of selected properties of the innermost mass trajectories in core-collapse supernova simulations of massive progenitor stars at two examples. The red dashed lines in the density graphs illustrate nuclear saturation density and the solid blue lines show the central data.

500 ms for all cases considered in this investigation. This is the central property of the quark matter description applied here due to the selective choice of parameters, which lead to the onset of the quark-hadron phase transition close to nuclear saturation density. Consequences with respect to the dynamical evolution will be further discussed below. The simulations are launched from low and intermediate mass Fe-core progenitors of 10.8 , 13 and $15 M_{\odot}$ from Woosley et al. (2002). First results from the 10.8 and the $15 M_{\odot}$ simulations have already been discussed in Sagert et al. (2009) and Fischer et al. (2010a). Here, we extend their analysis and present a deeper investigation with respect to the appearance of quark matter in PNS interiors and discuss consequences with respect to the neutrino signal emitted.

3.1. The early post bounce phase

The early post bounce phase of core-collapse supernovae of massive Fe-core progenitors is determined by an extended mass accretion period, during which the central density and temperature increase above several times nuclear density and above several tens of MeV. This behavior is shown in Fig. 8 for the example of the low-mass $10.8 M_{\odot}$ and the high-mass $40 M_{\odot}$ progenitor models, both using the (pure hadronic) EoS from Shen et al. (1998). Illustrated is the time evolution of selected mass trajectories, which belong to the PNS interiors, during the Fe-core collapse (see the radial evolution), bounce and the first 400 ms post bounce. Both models reach several times nuclear saturation density (red dashed lines in the density graphs) at bounce (i.e. at $t = 0$). They proceed in a similar fashion during the post bounce compression after the expanding bounce shock has come to halt. The central densities increase slowly above nuclear saturation density and reach $3.36 \times 10^{14} \text{ g/cm}^3$ (0.201 fm^{-3}) for the $10.8 M_{\odot}$ progenitor model and $3.99 \times 10^{14} \text{ g/cm}^3$ (0.238 fm^{-3}) for the $40 M_{\odot}$ progenitor model within the first 500 ms after bounce. Furthermore, the central elec-

tron fraction reaches low values, between $Y_e \simeq 0.28$ (at the center) and $Y_e \simeq 0.1$ near the neutrinospheres at intermediate densities around $10^{11} - 10^{13} \text{ g/cm}^3$. This highly deleptonized region originates from the launch of the deleptonization burst at about 5 ms post bounce (dominated by ν_e). Differences between these two progenitor models occur in the temperatures obtained during the first 400 ms post bounce evolution. The $10.8 M_{\odot}$ progenitor model in Fig. 8 (a) reaches temperatures of $T = 15 - 35 \text{ MeV}$ and the $40 M_{\odot}$ model in Fig. 8 (b) between $20 - 60 \text{ MeV}$. This effect is due to the more compact PNS obtained at bounce for the $40 M_{\odot}$ progenitor model and the larger mass accretion rate at the PNS surface.

3.2. The quark-hadron phase transition

We apply the hybrid EoS introduced in § 2.3 to core-collapse supernova simulations of massive Fe-core progenitor stars in spherical symmetry, where no explosions are obtained using standard hadronic EoSs from e.g. Lattimer & Swesty (1991) and Shen et al. (1998). In the following paragraphs, we illustrate the dynamical evolution obtained during the quark-hadron phase transition. We select as standard reference model, the $10.8 M_{\odot}$ progenitor model applying EOS2.

For this choice of parameters, quark matter appears at densities close to nuclear saturation density, where the critical density depends strongly on the temperature and the electron fraction obtained (see the discussion in § 2.3). The conditions permit quark matter already at core bounce, as illustrated in Fig. 9 (left panel). The corresponding hydrodynamic properties obtained are illustrated in Fig. 10. Quark matter appears at the center ($\leq 0.3 M_{\odot}$), at a mass fraction of about $\chi = 0.01 - 0.1$ (see the radial bounce profiles in Fig. 9 (left panel) and Fig. 10 for baryon density, electron fraction and temperature). The figures also show that down-quarks are the most abundant species, followed by strange-quarks and

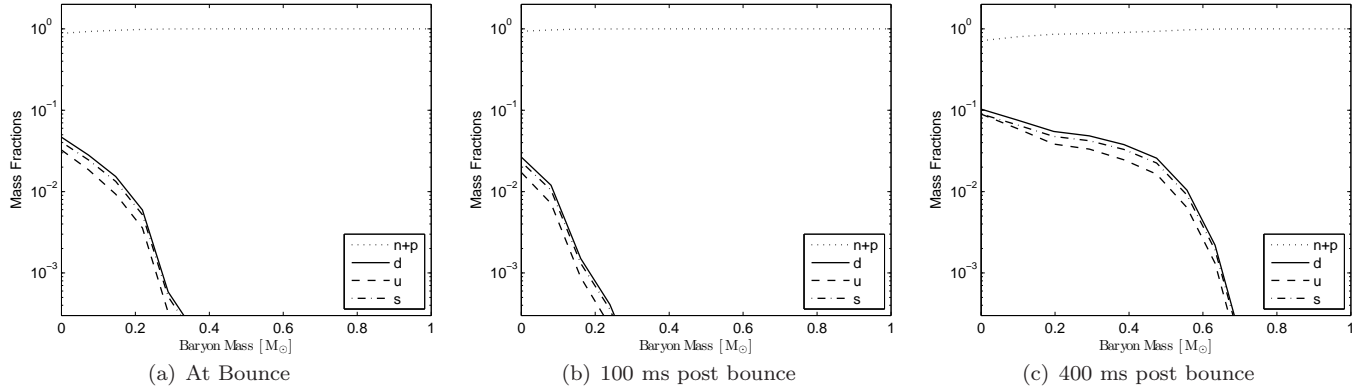


FIG. 9.— Evolution of the mass fractions of nucleons and the different quark flavors at bounce (left panel) and at the two selected post bounce times 100 ms (middle panel) and 400 ms (right panel) for the $10.8 M_{\odot}$ reference model.

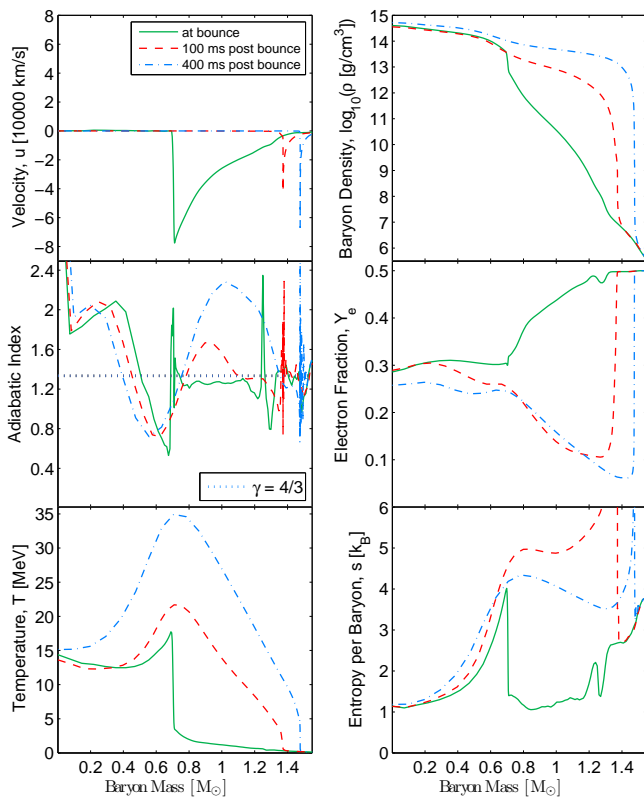


FIG. 10.— Radial profiles of selected hydrodynamic quantities during the appearance of quark matter for the $10.8 M_{\odot}$ reference model at bounce (solid lines) and at the two selected post bounce times 100 ms (dashed lines) and 400 ms (dash-dotted lines). The horizontal dotted line in the entropy graph illustrates the critical adiabatic index of $\gamma = 4/3$.

up-quarks, which can be understood as a consequence of charge neutrality and the low electron fraction at the center. This hierarchy remains during the later post bounce evolution. The small central fraction of quark matter reduces during the early post bounce expansion (see Fig. 9 (middle panel) and the radial profiles at bounce and at 100 ms post bounce in Fig. 10). Only after the dynamic bounce shock has stalled and the subsequent evolution is determined by mass accretion onto the PNS and heating behind the standing accretion shock (SAS), does the central density increase and the central electron fraction decrease. This in turn causes the quark matter volume

fraction to rise (see Fig. 9 (right panel) and Fig. 10 at 400 ms post bounce). The timescale for the quark matter fraction increase is given by the central density and temperature increase as well as by the electron fraction decrease. Hence it is determined by the mass accretion rate, which in turn depends on the progenitor model and the hadronic EoS (before the EoS is dominated by the quark contributions). For the massive Fe-core progenitors under investigation using the stiff EoS from Shen et al. (1998), the timescale is on the order of 100 ms , where a central density of $5.2 \times 10^{14} \text{ g}/\text{cm}^3$ and a temperature of 15 MeV are obtained (see Fig. 10). During the post bounce evolution, the adiabatic index γ decreases slowly below the critical value of $4/3$ on the same timescale, illustrated in Fig. 10. Furthermore, the appearance of quark matter at the PNS interior proceeds adiabatically as shown via the entropy per baryon profiles in Fig. 10. The PNS configuration is gravitationally stable as long as the maximum mass (given by the hybrid EoS) is not reached.

A quark matter volume fraction between 0 and 1 translates to matter in the quark-hadron mixed phase, for which the adiabatic index is reduced (see §2.3). This behavior is illustrated in Fig. 11 (c) at selected post bounce times, after the PNS exceeds its maximum stable mass and starts to collapse. The last stable configuration (it is not illustrated for simplicity) corresponds to the post bounce time of 428.5357 ms . The consequent softening of the EoS for matter in the mixed phase leads to a dramatic dynamical evolution. The reduced adiabatic index causes the mixed phase of the PNS to contract, as shown via the radial velocity profiles in Fig. 11 (a) during the collapse at three selected post bounce times. During the contraction, the central density and temperature increase (see Fig. 11 (b) and (e)). Furthermore, weak-equilibrium is established at a lower value of the electron fraction due to the changed thermodynamic conditions (see Fig. 11 (d)). The contraction accelerates and proceeds into an adiabatic collapse, during which the central entropy per baryon stays constant as shown in Fig. 11 (f). The central part of the PNS collapses sub-sonically and the outer part collapses super-sonically (similar to the Fe-core collapse). The timescale reduces from 100 ms to milliseconds. The compression results in significantly higher densities and temperatures, which in turn favors quark matter over hadronic matter. In this

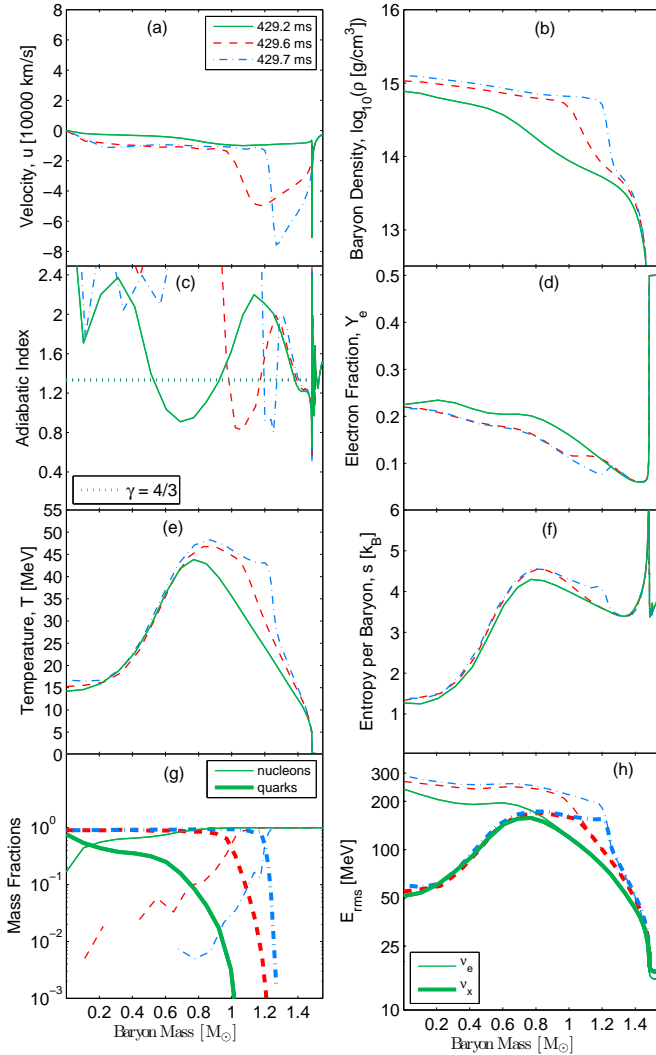


FIG. 11.— PNS collapse of the $10.8 M_{\odot}$ progenitor model due to the presence of quark matter, at three different post bounce times (solid lines: 429.2 ms, dashed lines: 429.6 ms, dash-dotted lines: 429.7 ms) after the PNS has become gravitationally unstable. The same configuration as Fig. 9 but in addition graphs (g) and (h) show the mass fractions of nucleons (thick red lines) and quarks (thin blue lines) and the mean energies for ν_e (thin lines) and for (μ/τ) -(anti)neutrinos (thick lines), respectively.

sense, the quark-hadron phase transition which started slowly on timescale of 100 ms proceeds rapidly during the PNS collapse until the pure quark matter phase at the PNS center grows and a quark core of about $1.3 M_{\odot}$ is formed (see the composition in Fig. 11 (g)). The quark fractions of up-, down- and strange-quarks rise equally whereas in the pure quark-matter phase down-quarks and strange-quarks are favored over up-quarks (see Fig. 9). This is due to the fact that the chemical potentials are equal for s-quarks and d-quarks (see § 2.3) and matter is neutron-rich. The different symmetry energy for quark matter, together with the higher densities and temperatures obtained during the PNS collapse, result in a different weak-equilibrium where Y_e is generally lower. The lower Y_e obtained (see Fig. 11 (d)) between $0.8 - 1.3 M_{\odot}$ reduces the pressure of the degenerate electron gas and hence softens the EoS additionally, which in turn supports the collapse. In addition, the mean neu-

trino energies are also shifted to higher values, where the electron flavor neutrinos are most sensitive to density variations. As shown in Fig. 11 (h), the central mean energies of the electron neutrinos increase from about 250 MeV before the PNS collapse to about 300 MeV. The largest increase of the mean electron neutrino energy was found for the infalling material where density and temperature increase most, from 10^{14} g/cm^3 to 10^{15} g/cm^3 and from 15 MeV to 45 MeV (see Fig 11 (b) and (e)). There, the mean neutrino energy increases from about 75 MeV to about 200 MeV for ν_e and to about 150 MeV for the $(\nu_{\mu/\tau}, \bar{\nu}_{\mu/\tau})$. A less pronounced increase of the mean neutrino energies can be found for the (μ/τ) -(anti)neutrinos, which rise from about 50 MeV to about 60 MeV at the center. The mean free paths of all neutrinos are extremely small, on the order of few 10 – 1000 cm. Hence the neutrinos are highly trapped and cannot escape on the timescales on the order of milliseconds up to hundreds of milliseconds that are found during the post bounce PNS evolution.

As discussed in §2.3, the adiabatic index rises again in the pure quark phase. This behavior is illustrated in Fig. 11 (c) during the PNS collapse. The obtained quark core and the consequent stiffening of the EoS for matter in the pure quark phase at the PNS interior, causes the PNS collapse to halt. A strong hydrodynamic shock forms, which can be identified in the radial velocity profile at $t = 429.6 \text{ ms}$ post bounce in Fig. 11 (a) and the entropy increase in Fig. 11 (f). The shock wave forms at about $1.25 M_{\odot}$. The system does not overshoot its hydrostatic equilibrium configuration, because quark stars (or hybrid stars with extended strange quark cores) are energetically self bound objects, the total internal energy becomes larger than the gravitational binding energy, at the densities considered here (for a detailed discussion, see e.g. § 18 in Weber 1999). Hence, the scenario cannot be considered a second bounce. Furthermore, when the shock reaches the sonic point it still remains a pure accretion front with no matter outflow, as shown in the Figs. 11 and 12(a).

The shock forms due to the stiffening of the EoS in the pure quark phase and due to the supersonically infalling outer part, which does not know about the halted collapse at the center. Information about the central stiffening cannot propagate outward across the sonic point. Initially, the second shock wave appears as a standing accretion front with no matter outflow (see Fig. 11 (a)). The shock evolution is given by the balance of ram-pressure ahead of the shock from the infalling nucleons and the thermal pressure from the dissociated quarks behind the shock. The shock position determines the phase boundary between the quark-hadron mixed and the pure hadronic phases, due to the large density and temperature jumps at the shock front. The dissociated nuclear matter, which accumulates onto the PNS surface, has been shock heated at the SAS previously. As this dissociated material crosses through the second accretion shock, it is converted from hadronic matter to quark matter. For all our models, the second accretion shock was found to propagate outward towards the PNS surface (see the radial velocity profiles in Fig. 12(a) (a) at the example of the $10.8 M_{\odot}$ progenitor reference model). Thereby, the outwards propagating shock wave remains a

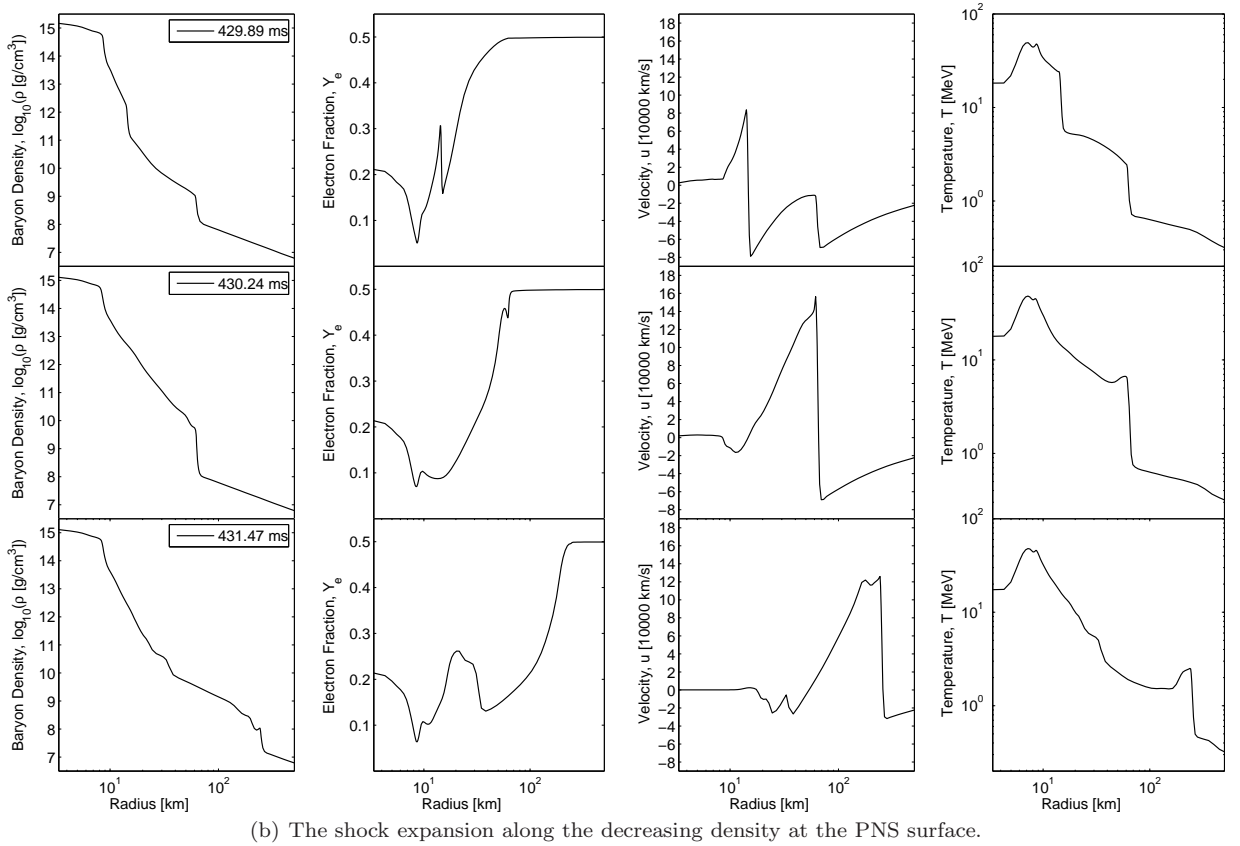
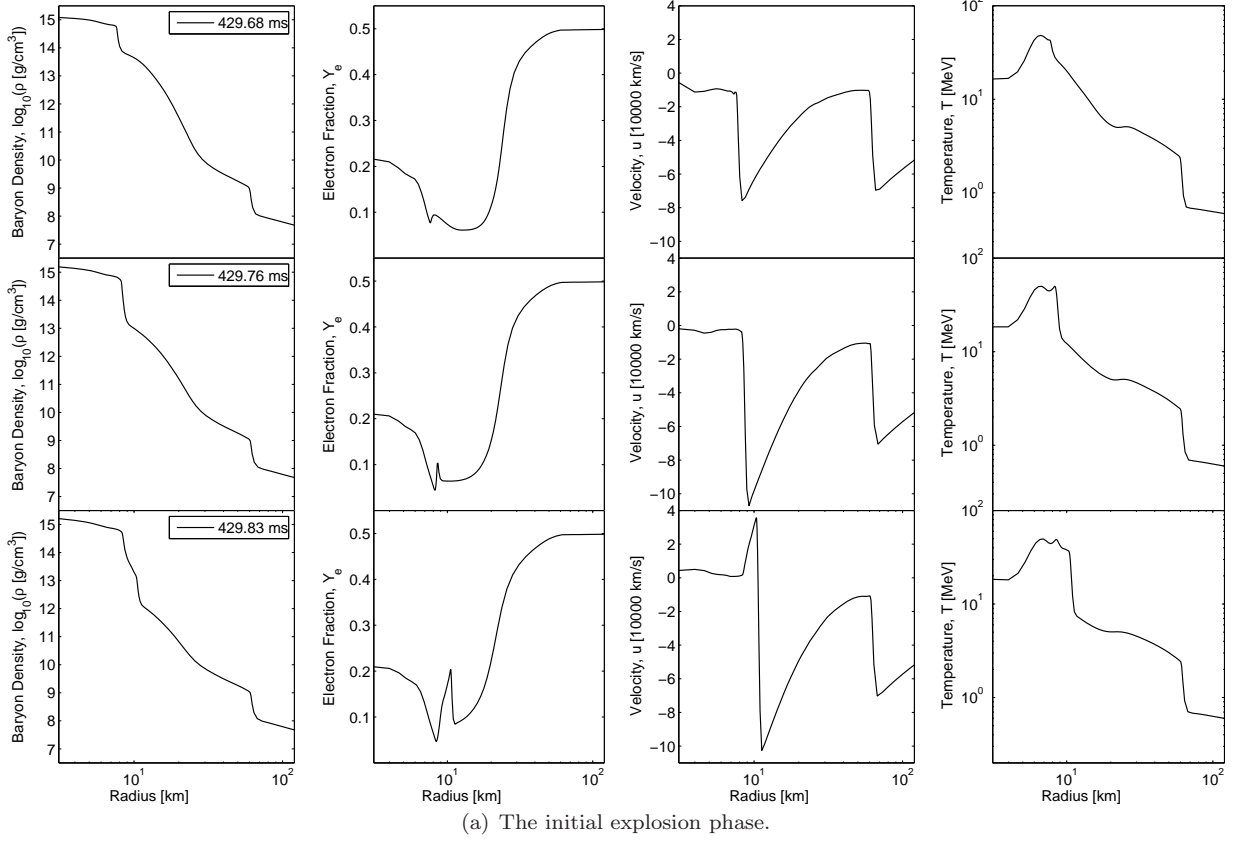


FIG. 12.— Radial profiles of selected hydrodynamic variables during the explosion of the $10.8 M_{\odot}$ reference model due to the quark hadron phase transition, at selected post bounce times.

pure accretion front with no matter outflow, as shown in Fig. 11 (a) between 429.6 ms and 429.7 ms post bounce and in Fig. 12(a) at 429.68 ms and 429.83 ms.

The density and temperature jumps at the shock increase, as long as it remains a pure accretion front. Mass from the outer gravitationally unstable part of the PNS continues to fall onto the shock front, increasing the infall velocities at the shock (see the velocities in the middle panel of Fig. 12(a)). The material accumulates onto the central quark core. The increasing thermal pressure behind the standing shock front drives the shock slowly outwards, supported by the increasing heating right behind the standing accretion shock illustrated in Fig. 13(a). In the presence of the largely enhanced $\bar{\nu}_e$ -luminosity, $\bar{\nu}_e$ -absorption at protons dominates over ν_e -absorption at neutrons, even though the conditions are generally neutron-rich. The sharp rise of the heating rates just behind the shock corresponds to the increasing Y_e illustrated in the Fig. 12(a). Behind the heating region, small (in comparison to the heating at the shock) cooling rates dominate (see Fig. 13(a)).

As the density of the infalling material decreases it becomes too low for hadronic matter to be converted into quark matter. At the phase boundary between the quark-hadron mixed phase and the pure hadronic phase, the density decreases from about 10^{15} g/cm³ to about 10^{14} g/cm³ (see the lower panel of Fig. 12(a)). Eventually, the shock wave detaches from the surface of the PNS and accelerates. Positive matter velocities are obtained, where where the accretion front turns into a dynamic shock wave. Because the density at the PNS surface decreases also at larger radii, from 10^{14} g/cm³ at the phase boundary between the mixed and the hadronic phases to 10^{10} g/cm³ at the low density envelope, the shock continues to accelerate (see Fig. 12(b)). Velocities on the order of $1 - 1.5 \times 10^5$ km/s are obtained during the shock passage across the low density envelope. The scenario is again different from the early shock propagation of the bounce shock, where the shock suffers immediately after its formation from the dissociation of infalling heavy nuclei which causes an energy deficit of about 8 MeV per baryon. Here, the infalling matter is already dissociated and composed of only free nucleons and light nuclei. In this sense, the shock does not lose energy during the initial propagation. Even more, during the initial shock expansion neutrino heating still deposits energy behind the shock wave (see Fig. 13(a) and compare with Fig. 12(a) as well as Fig. 13(b) and compare with Fig. 12(b)).

The expanding dynamic shock wave finally merges with the SAS from the Fe-core bounce (see Fig. 12(b) at $t = 430.24$ ms post bounce), which remained unaffected from the events inside the PNS at a radius of about 80 km. Maximum matter outflow velocities of 1.6×10^5 km/s are obtained. The initial shock expansion slows down when the dynamic shock wave reaches infalling heavy nuclei from the outer layers after merging with the standing accretion shock from core bounce. The matter velocities decrease continuously during the later evolution to typically $4 - 6 \times 10^4$ km/s (depending on the progenitor model). However, for all models under investigation the expanding shock wave was never found to stall again at later times. Hence, the quark-hadron phase transition triggers not only the formation

of a strong additional shock wave but also launches an explosion in core-collapse supernova simulations where otherwise no explosions could be obtained.

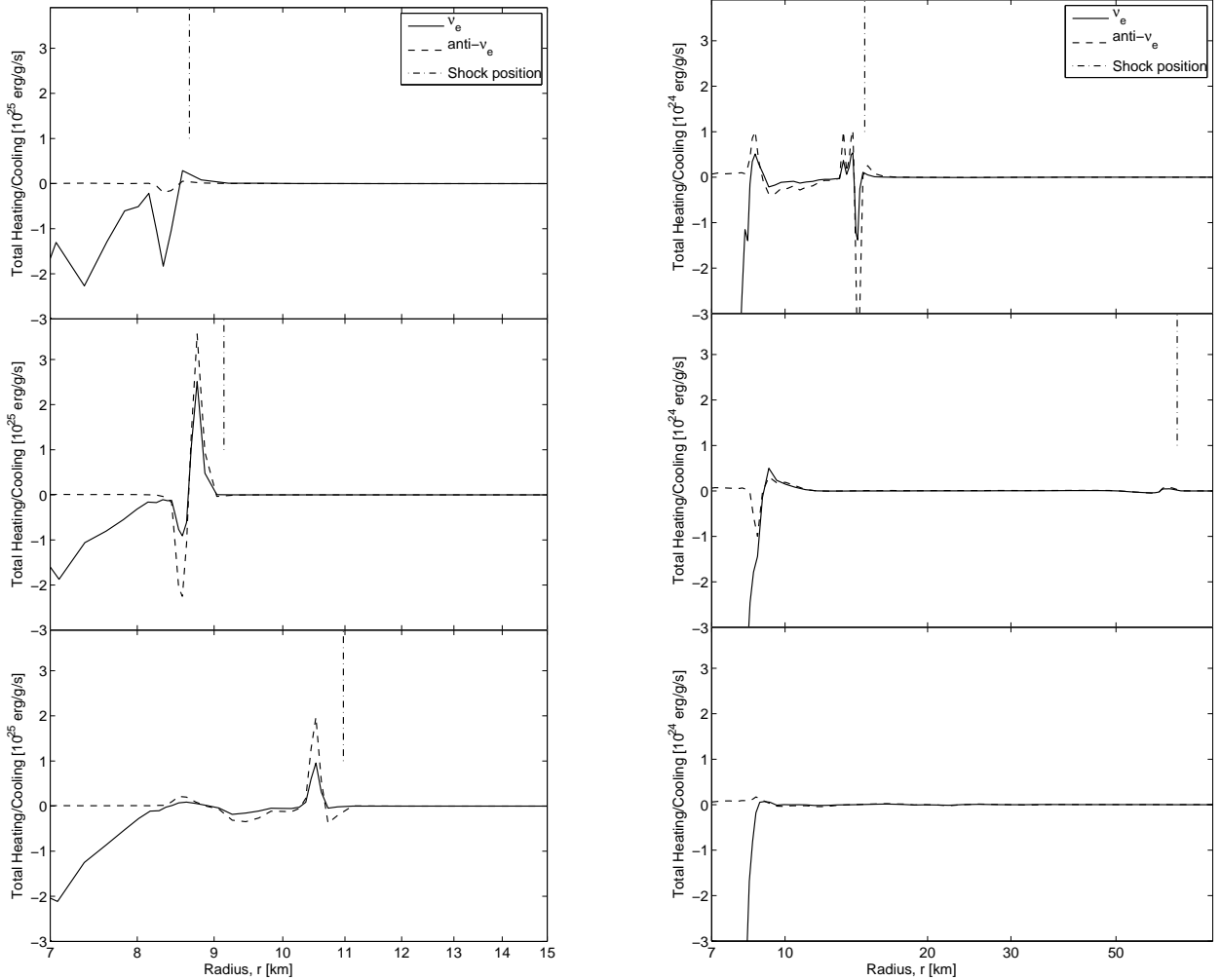
3.3. The neutrino observables

First, we describe the standard neutrino signal obtained from a failed core-collapse supernova explosion of $10.8 M_\odot$ using the pure hadronic EoS from Shen et al. (1998). Below, we will compare these neutrino spectra with the spectra obtained taking QCD degrees of freedom into account.

The evolution of the neutrino luminosities and root-mean-square energies are shown in Fig. 14 (a) for the $10.8 M_\odot$ progenitor model using the standard hadronic description of nuclear matter, measured at a distance of 500 km in the co-moving reference frame (for a definition of the neutrino observables, see Fischer et al. 2010b). During the deleptonization burst at bounce, the electron neutrino luminosity rises up to several 10^{53} erg/s on a timescale of 5 – 20 ms post bounce. $\bar{\nu}_e$ are produced only after bounce due to the decreased degeneracy which allows, next to electrons, also for positrons and the corresponding charged current reactions as well as pair-processes. The same holds for (μ/τ) -neutrinos, which are produced only via pair-processes after bounce. The early (on timescale of 100 ms post bounce) evolution of the neutrino spectra is given by the balance of mass accretion and diffusion at the neutrinospheres. After the deleptonization burst has been launched, the electron-flavor neutrino luminosities increase slightly until about 150 ms post bounce, due to the moderately large mass accretion rate. The (μ/τ) -neutrino luminosities decrease constantly with time because their spectra are given by diffusion rather than by accretion. The electron flavor luminosities follow the same decreasing behavior after the mass accretion rate at the neutrinospheres drops below a certain threshold (depending on the progenitor model). At 400 ms post bounce, the electron-flavor (μ/τ) -neutrino luminosities reach values of about 5×10^{52} (3×10^{52}) erg/s. The mean energies of the electron-flavor neutrinos increase continuously with respect to time after bounce, from 10 (15) MeV after the deleptonization burst has been launched to 14 (17) MeV at 400 ms post bounce. The mean energies of the (μ, τ) - (anti)neutrinos decrease slightly with time after bounce and reach about 19 MeV at 400 ms (see Fig. 14 (a)).

The evolution of the neutrino observables from the simulations applying the hybrid EoS introduced in §2.3, is shown in Fig. 14 (b) for the $10.8 M_\odot$ progenitor reference model. Compared to the standard hadronic scenario, we find very similar spectra for post bounce times before the PNS collapse (see Fig. 14 (b)). Differences occur in slightly higher neutrino luminosities, which are due to the more compact PNS where quark matter is present.

The propagation of the second shock wave across the neutrinospheres releases an additional burst of neutrinos, where neutrinos of all flavors carry away energy on the order of several 10^{53} erg/s on a short timescale on the order of a few milliseconds. The scenario is similar to the bounce shock propagation across the neutrinospheres where the deleptonization burst is released which, however, appears only in ν_e . In order to understand the release and the nature of the second burst as shown in Fig. 14 (b) at about 430 ms after bounce, we



(a) At 429.68 ms, 429.76 ms and 429.83 ms post bounce (from the top to the bottom), which correspond to the post bounce times shown in Fig. 12(a).

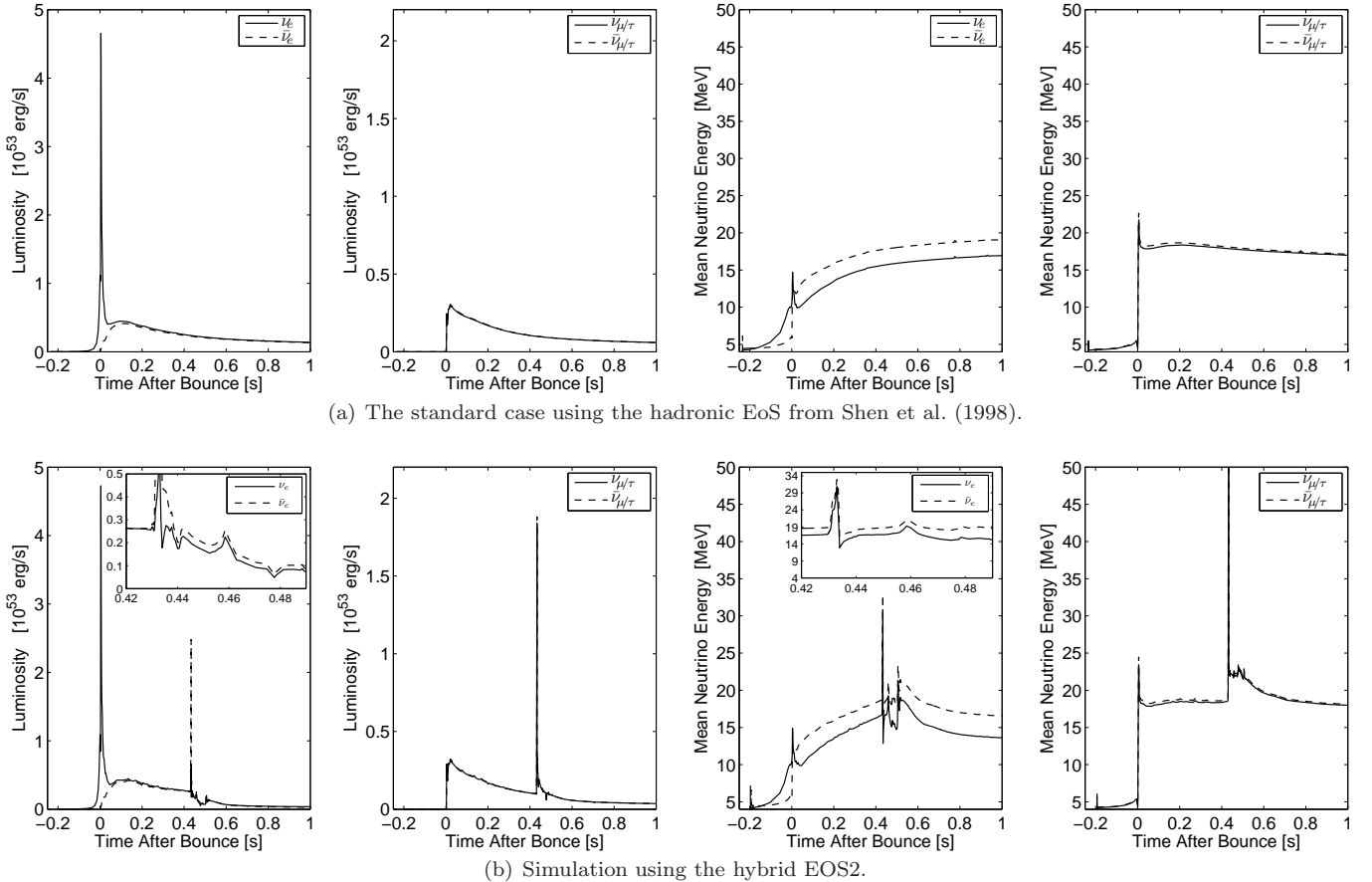
(b) At 429.89 ms, 430.24 ms and 431.47 ms post bounce (from the top to the bottom), which correspond to the post bounce times shown in Fig. 12(b).

FIG. 13.— Total net heating/cooling rates for ν_e (solid lines) and $\bar{\nu}_e$ (dashes lines) at selected post bounce times. Negative (positive) values correspond to a net cooling (heating). The vertical dash-dotted lines show the position of the expanding explosion shock.

must consider what happens when the expanding second shock wave passes through the formerly dissociated and now again shock heated nucleons. Material at the PNS surface has an electron fraction of $Y_e \simeq 0.1$. This low Y_e stems from the deleptonization burst shortly after core bounce (see Fig. 12(a)). The heating by the shock lifts the electron degeneracy (compare Figs. 12(a) and 12(b)). It allows for the creation of electron-positron pairs followed by positron captures on neutrons that increase the electron fraction. This can be clearly identified via the reduced degeneracy of the infalling material ahead of the shock during the initial shock expansion, as long as the shock front remains a standing accretion shock (see Fig. 15 (a)). The situation changes when the shock accelerates at the PNS surface to positive velocities (see Figs. 12(a) and 12(b)). The degeneracy of the infalling material reduces significantly at the shock front (see Fig. 15 (b)). On the other hand, the degeneracy of the matter that accumulates behind the shock increases. Hence, the electron fraction of the infalling material decreases while the electron fraction behind the shock increases (see Fig. 12(a)). Note that the same behavior for

the electron degeneracy discussed here and shown in the Figs. 15 (a) and (b) (left panel), holds for the charged chemical potential $\mu_n - \mu_p$, which is shown in the Figs. 15 (a) and (b) (right panel). The charged chemical potential decreases ahead of the expanding shock front and increases behind it.

The shock passage across the neutrinospheres (see the vertical lines in Fig. 15) releases the second neutrino burst. The increasing temperature enhances the production of electron-positron pairs, where most of the positrons are captured by neutrons producing a burst of electron antineutrinos. Some positrons interact via pair process (7) from Table 1, contributing to all neutrino species. This explains why the second neutrino burst is dominated by $\bar{\nu}_e$ while ν_e and $(\nu_{\mu/\tau}, \bar{\nu}_{\mu,\tau})$ have similar luminosities (see Fig. 14 (b)). The electron (anti)neutrino luminosities increases from 0.2611×10^{53} (0.2708×10^{53}) erg/s to 0.55×10^{53} (2.2×10^{53}) erg/s on a short timescale on the order of milliseconds. The same increase in luminosity holds for the (μ/τ) -neutrinos, which reach about 1.5×10^{53} erg/s. The sharp peak of the



(a) The standard case using the hadronic EoS from Shen et al. (1998).

(b) Simulation using the hybrid EOS2.

FIG. 14.— Evolution of the neutrino luminosities and mean neutrino energies for the $10.8 M_{\odot}$ progenitor model with respect to time after bounce, comparing the standard hadronic EoS from Shen et al. (1998) and the hybrid EOS2. The data are measured at a distance of 500 km in the co-moving reference frame.

neutrino luminosities is accompanied by a sharp rise of the mean neutrino energies. The electron (anti)neutrino mean energies increase from 16.5 (18.4) MeV to 29.38 (32.2) MeV, and the mean (μ/τ) -neutrino energies rise from about 18.5 MeV to 53.7 MeV on the same short timescale on the order of milliseconds.

The later evolution of the PNS surface is shown in Fig. 16 via the radial profiles of ρ , Y_e , velocity and T at selected post bounce times during the ongoing explosion phase. Neutrino cooling after the shock propagation across the neutrinospheres (see Fig. 13(b)) leads to the establishment of matter infall between the expanding explosion shock and the PNS surface already at about 430.24 ms after bounce in Fig. 12(b) between 10–20 km. As matter continues to fall onto the PNS surface with even supersonic velocities, an additional accretion shock forms at the PNS surface. This additional accretion shock on top of the PNS surface expands due to neutrino heating and falls back due to cooling (see therefore the large cooling rates between 7–10 km in Fig. 13(b)) on timescales on the order of 10 ms, during which the neutrinospheres expand and contract correspondingly. The same phenomena apply as discussed in the paragraph above. The shock propagation towards the neutrinospheres increases the temperature at the neutrinospheres, where the enhanced opacities cause the propagation of the neutrinospheres to lower densities. Neutrino cooling, as well as the obtained matter expansion at

the neutrinospheres, shifts the neutrinospheres to higher densities. The consequently increasing and decreasing mass accretion rate is reflected in the electron flavor neutrino luminosities and mean energies, shown in the insets in Fig. 14 (b) after the second neutrino burst between 432–500 ms.

The additional standing accretion shock, propagating back and forward at the PNS surface, settles down to a quasi-stationary state at about 550 ms post bounce. After that, the evolution of the neutrinospheres is determined by mass accretion on the order of few $0.1 M_{\odot}/s$ at a timescale on the order of 100 ms up to seconds. The neutrino luminosities decrease to values below 10^{52} erg/s within the first 500 ms after the onset of the explosion. The mean neutrino energies follow the same behavior. The mean electron (anti)neutrino energies decrease from about 18 (20) MeV at 550 ms post bounce to 12 (18) at 1 second post bounce (see Fig. 14 (b)). The mean (μ/τ) neutrino energies decrease only slightly from 22 MeV at 550 ms post bounce to about 19 MeV at 1 second post bounce. Unaffected by the behavior of the standing accretion shock at the PNS surface, the explosion shock continues to expand to larger radii with matter velocities on the order of several 10^4 km/s (see Fig. 16).

4. DISCUSSION

In this section, we will compare the results obtained using the $10.8 M_{\odot}$ reference model with the remaining sim-

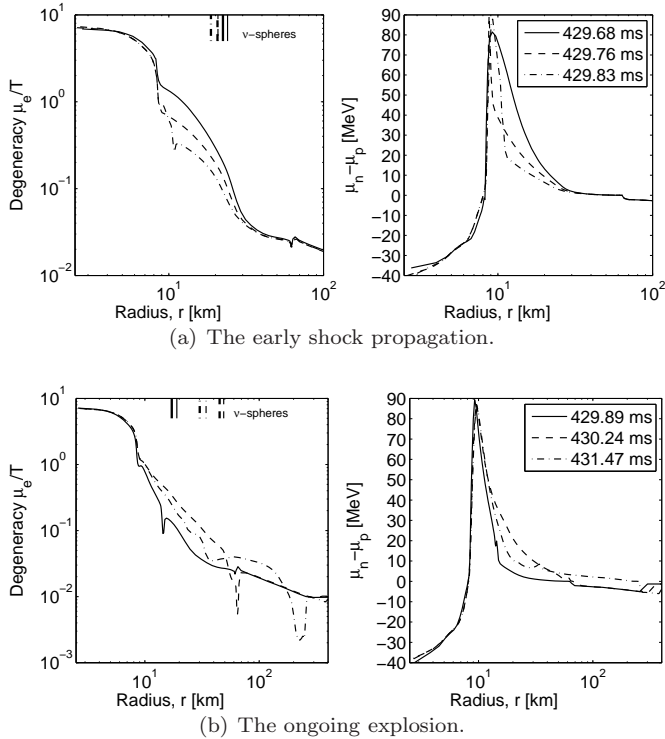


FIG. 15.— Radial profiles for the degeneracy parameter $\eta = \mu_e/T$ and charged chemical potential $\mu_n - \mu_p$ for the selected post bounce times of Figs. 12(a) and 12(b).

ulations that have been performed where different progenitor models as well as different quark EoS parameters are used. Further below, we will discuss possible applications with respect to the PNS structure and the formation of magnetars as well as with respect to possible nucleosynthesis investigations.

TABLE 2
SUMMARY OF THE MODELS UNDER INVESTIGATION.

Prog. [M_\odot]	EoS	t_{pb} [ms]	ρ_c^a [10^{14} g/cm 3]	T_c^a [MeV]	Y_e^a
10.8	EOS1	240	6.607	13.14	0.234
10.8	EOS2	428	6.457	14.82	0.237
13	EOS1	235	6.493	13.32	0.235
13	EOS2	362	7.228	16.38	0.191
15	EOS1	172	7.523	17.15	0.170
15	EOS2	275	7.586	16.25	0.187
15	EOS3	308	5.511	17.67	0.197

^a Selected central properties of the PNSs at the onset of collapse (t_{pb}).

4.1. Explosions in spherical symmetry

In addition to the low-mass reference model of $10.8 M_\odot$, we apply the hybrid EoSs introduced in § 2.3 to core-collapse supernova simulations of the intermediate mass Fe-core progenitor stars of 13 and $15 M_\odot$ from Wosley et al. (2002). The results are summarized in Table 2. We list the characteristic properties of the simulations for the different progenitor models and the hybrid EoSs with the two different values of the bag constant. The values t_{pb} are the post bounce times when the PNSs become gravitationally unstable and start to

collapse. The corresponding central conditions, i.e. density ρ_c , temperature T_c and electron fraction Y_e , are also listed⁴. The models using the larger bag constant, which corresponds to a higher critical density, reach typically lower quark volume fractions at equal evolutionary states post bounce. In order to reach similar central densities, the PNSs have to accrete more mass which leads to a longer accretion time post bounce. This effect is compensated by the lower maximum stable mass of the configurations using the larger bag constant. Hence, the central densities required for the PNSs to become gravitationally unstable and collapse are rather similar for the same progenitor model. On the other hand, due to the longer mass accretion period for the models using the larger bag constant on the order of 100 – 200 ms, the PNSs are more compact before collapsing. In addition, the central temperatures obtained are higher by about 2 – 3 MeV. This in turn favors quark matter over hadronic matter (see the phase diagrams in Fig. 4(a)–5(c) in § 2.3), where weak-equilibrium is established at a lower value of the electron fraction (see Table 2).

All models listed in Table 2 evolve in a similar fashion during the quark-hadron phase transition. The explosions are obtained due to the formation of the strong second hydrodynamic shock front inside the PNSs. The shocks accelerate at the PNS surfaces, i.e. the shock breakout, which triggers the explosions where otherwise no explosions could have been obtained in spherical symmetry. The explosion energy estimates E_{expl} and approximate neutron star masses M_{NS} (for a definition of the mass cut and the explosion energy, see Fischer et al. 2010b, following a suggestion by S. Bruenn), are listed in Table 3. Moderate explosion energies of about 1×10^{51} erg could be obtained for the reference model, i.e. $10.8 M_\odot$ using the hybrid EOS2. The models with an early PNS collapse and hence the early onset of the explosion reach smaller explosion energies. The shorter mass accretion period post bounce lead to less compact PNS configurations and therefore less steep density gradients at the PNS surfaces until they become gravitationally unstable and collapse due to the presence of quark matter in the interiors. The comparison of the two hybrid EOS1 and EOS2 ($\alpha_S = 0$) is shown in Fig. 17 for the $10.8 M_\odot$ progenitor model. The PNS obtained for $B^{1/4} = 165$ MeV (EOS2) is more compact, indicated by the more massive quark core in Fig. 17 (f) of about $0.15 M_\odot$ at the moment of shock breakout. It results in the higher density and temperature shown in the Figs. 17 (e) and (b). Furthermore, the longer mass accretion time for the model using $B^{1/4} = 165$ MeV (EOS2) relates to lower densities and a steeper density gradient, surrounding the central quark core of the PNS (see Fig. 17 (b)) at the moment of shock breakout. This allows for a stronger shock acceleration of the second shock wave expanding along the decreasing density gradient at the PNS surface. These differences are the origin of the higher explosion energy estimates using EOS2 in comparison to EOS1. Hence, the acceleration of the formed hydrodynamic shock at the PNS surface is less intense for the models using the low bag constant. Lower explosion energies are also obtained for the more massive progenitors.

⁴ Note that the values of ρ_c , T_c and Y_e are not the critical conditions for the appearance of quark matter.

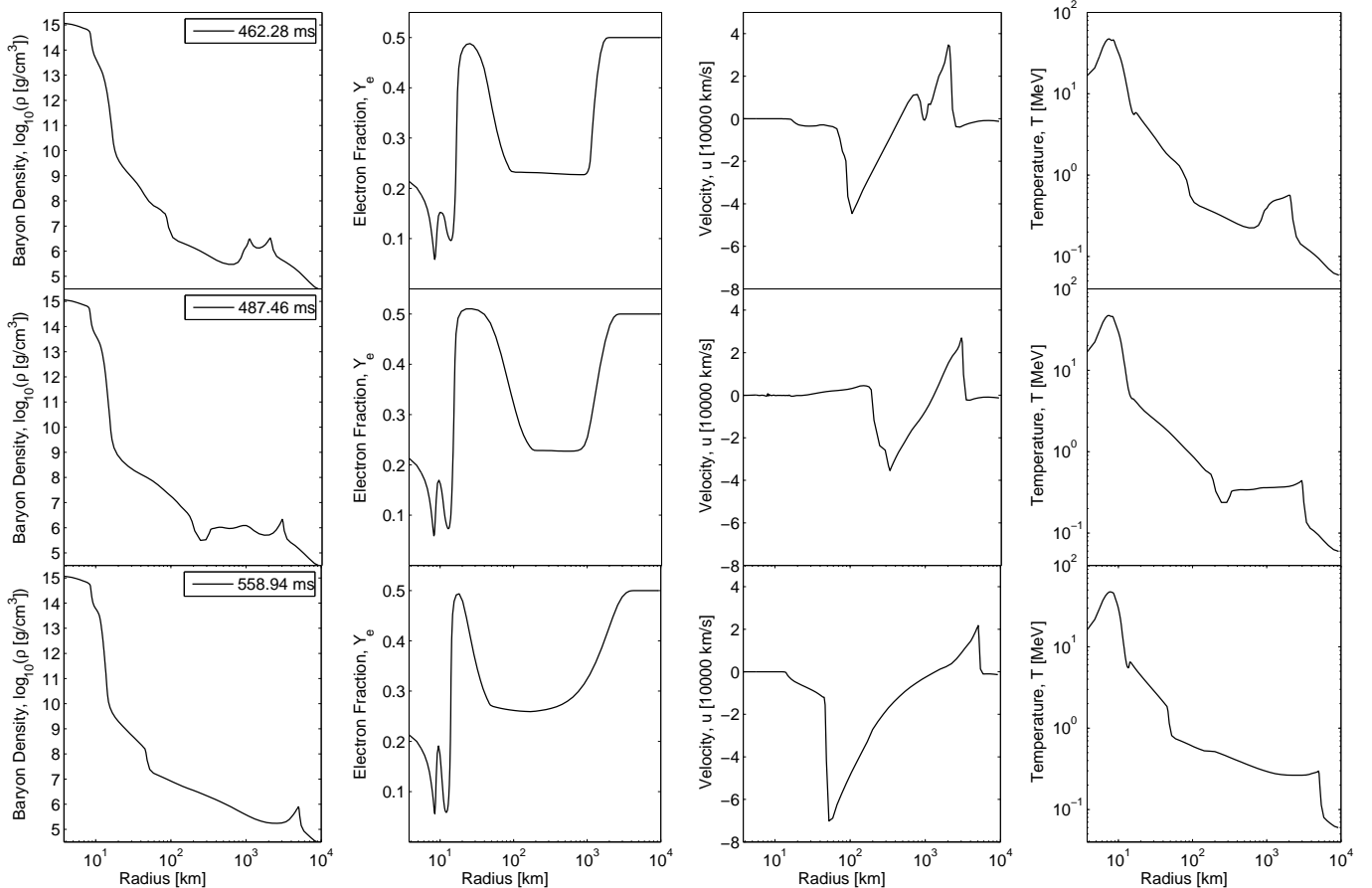


FIG. 16.— Selected radial profiles for the $10.8 M_{\odot}$ reference model during the ongoing explosion phase at three late times post bounce. Illustrating is the back and forth propagating accretion shock at the PNS surface established via to neutrino cooling/heating.

The more massive envelopes of the PNSs with significantly higher densities prevents a similar strong shock acceleration. In general, the explosion energy estimates may be lifted to larger values if multi-dimensional phenomena (e.g. convection and rotation) are taken into account.

4.2. PNS collapse to a black hole

A special model is the $15 M_{\odot}$ progenitor, using the hybrid EOS2 (see Table 2). The evolution of this model is shown in Fig. 18 via radial profiles of velocity, density and temperature in the graphs (a), (b) and (c) respectively at four selected post bounce times. The graphs illustrate the last stable configuration as well as the PNS collapse. The evolutionary scenario, i.e. the PNS collapse due to the softening of the EoS in the mixed phase and the subsequent shock formation due to the stiffening of the EoS in the pure quark phase (clearly identified via the velocity, density and temperature profiles in Fig. 18 (a), (b) and (c) respectively at the first three post bounce times), is in qualitative agreement with the reference case discussed in § 3. During the shock propagation towards the PNS surface, mass accretion onto the second shock wave continuously increases the central density and hence the quark core of the PNS grows in mass. When the maximum stable mass (given by the hybrid EoS) of the configuration is reached, the PNS collapses a second time as shown in Fig. 18 (dotted-lines). Relativistic effects become more and more important. This is illustrated in

Fig. 18 (d) via the metric function $\alpha(t, a) = g_{tt}$, i.e. the lapse function, which approaches zero. It indicates the appearance of the event horizon and hence the formation of a black hole. By our choice of a co-moving coordinate system, stable solutions for the evolution equations of energy and momentum cannot be obtained. Hence, the simulations cannot be continued beyond that point.

The evolution scenario of black hole formation induced via the PNS collapse found via the hybrid EoS here is in qualitative agreement with the results obtained by Nakazato et al. (2008b) and Nakazato et al. (2010b) for very massive stars of $100 M_{\odot}$ and for the $40 M_{\odot}$ progenitor from Woosley & Weaver (1995). Furthermore, the results agree qualitatively with the pure hadronic scenario of black hole formation discussed by Suniyoshi et al. (2007) and Fischer et al. (2009) for several massive progenitor stars in the mass range of 40 – $50 M_{\odot}$. Differences occur in the larger maximum masses for the hadronic EoS.

4.3. Robustness of the observable features

The peak-like rise of the luminosities and mean neutrino energies is an indirect consequence of the quark-hadron phase transition as discussed for the reference case in § 3. It was found to occur for all models under investigation. The results are shown in Figs. 19 and 20 for the models using the hybrid EOS1 (in graphs (a)) and EOS2 (in graph (b)). The different post bounce times t_c (as listed in Table 3 together with the corresponding cen-

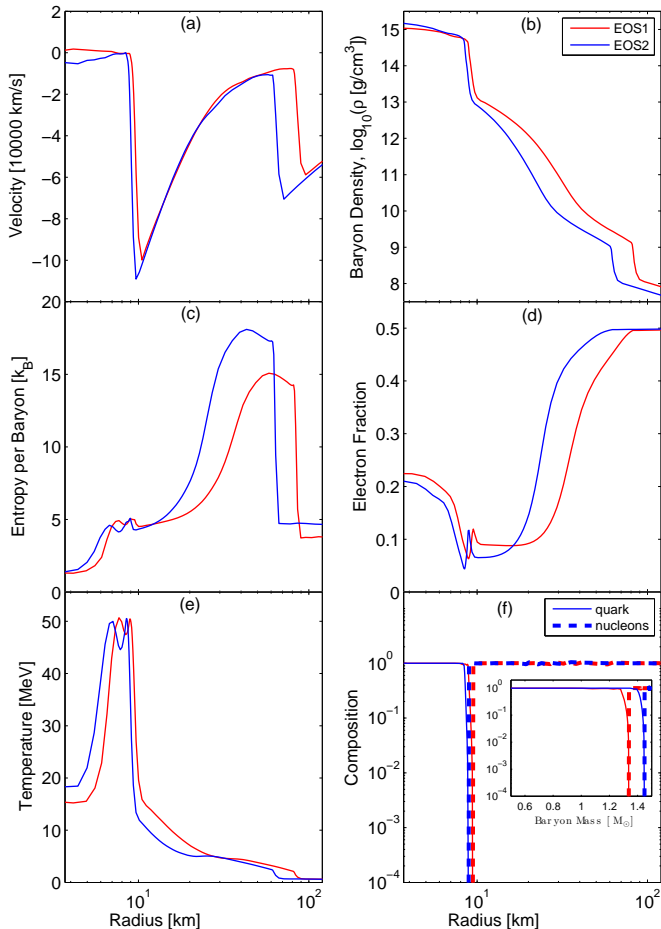


FIG. 17.— Selected radial profiles for the $10.8 M_{\odot}$ progenitor model, comparing the hybrid EOS1 (red lines, at 248.57 ms post bounce) and EOS2 (blue lines, at 429.76 ms post bounce), both at the moments just before shock breakout along the decreasing density at the PNS surfaces. Graph (f) shows the composition, i.e. quark volume fraction (solid lines) and the hadronic matter (dashed lines). In addition to the radial profile in graph (f), the inset shows the composition with respect to the baryon mass.

tral maximum densities ρ_{\max}) for the appearance of the second peak and the magnitude of the peaks depend on the microphysics and the progenitor model. The quantity ρ_{\max} relates to the maximum central density obtained at the end of the PNS collapse.

For all models under investigation (see Fig. 19 and 20), the luminosities and mean neutrino energies follow a similar behavior. After a sharp rise on timescales on the order of milliseconds, the luminosities and mean neutrino energies increase and decrease in accordance to the expanding and descending standing accretion shock at the PNS surface, between 10–50 ms after the burst. A quasi-stationary state is obtained after about 100 ms after the sharp rise. The luminosities and mean neutrino energies decrease continuously indicating the ongoing explosions. All models evolve in a similar fashion as discussed in § 3, through the PNS collapse and the subsequent evolution. Hence, the second peaks are dominated by $\bar{\nu}_e$ and $(\nu_{\mu/\tau}, \bar{\nu}_{\nu/\tau})$ for all models under investigation (see Fig. 19). Furthermore, the bursts are accompanied by significant increase of the mean neutrino energies (see Fig. 20).

The magnitude and the width of the luminosities and

mean neutrino energies of the second neutrino burst found are on the same order for all models under investigation, independent of the progenitor model and independent of the bag constant. On the other hand, the onsets for the second neutrino bursts take place at different times post bounce and depend on both the progenitor model and the bag constant. As shown in the Figs. 19 and 20, the second neutrino bursts for the $10.8 M_{\odot}$ and $13 M_{\odot}$ models using EOS1 occur at similar times because the conditions for the PNSs to become gravitationally unstable are obtained at similar post bounce times (see Table 2). Since the structure of these two progenitor models is relatively similar, they evolve in a similar fashion and on a similar timescale post bounce until the PNSs collapse. The $15 M_{\odot}$ progenitor model on the other hand is more compact and the conditions for the PNS collapse using EOS1 are obtained slightly earlier by about 40 ms (see Table 2 and compare with the post bounce time of the second neutrino burst in Figs. 19 and 20 (a)).

The simulations using the hybrid EOS2 is shown in the Figs. 19 (b) and 20 (b). They bring the differences between the progenitor models to light, due to the different post bounce accretion times before the PNSs become gravitationally unstable and collapse. The lower progenitor masses relate to longer accretion times and hence later second neutrino bursts. The delay for the different models explored in this article is on the order of about 100 ms for the 10.8 to the 13 as well as between the 13 and $15 M_{\odot}$ progenitor models. In other words, the differences between the post bounce times for the release of the second neutrino bursts relate to the same critical conditions for the quark-hadron phase transition but different evolutionary scenarios due to the different progenitor models. The future observation of such multi-peaked neutrino spectra might allow us to extract fundamental information about the state of matter at extreme conditions. The magnitude of the second burst and its delay after the deleptonization burst after core bounce contains information about the quark and hadron EoSs. If the progenitor model is known and the pure hadronic EoS is fixed, it may be possible to extract the critical conditions for the quark-hadron phase transition from the observed neutrino signal. The post bounce times for the release of the second neutrino burst and the corresponding central conditions for the PNS collapse are listed in Table 2 for all models under investigation. First results have been analyzed with respect to the possible observation of such a neutrino burst by Dasgupta et al. (2010) based on results discussed in Sagert et al. (2009), exploring the $10.8 M_{\odot}$ progenitor model where the hybrid EOS1 was used. They find that the operating neutrino detectors, Super-Kamiokande and IceCube, could detect such a $\bar{\nu}_e$ -burst from a future Galactic event.

4.4. Corrections of the strong coupling constant

Massive stars of $15 M_{\odot}$ are in the expected mass range of exploding progenitors, that result in stable PNSs at least during the time of explosion. The evolutionary scenario of black hole formation applying the hybrid EOS2 as discussed above in § 4.2, indicates that important ingredients are missing. For that particular model, the PNS collapses to a black hole because the maximum stable mass of the configuration, which is given by the hybrid EoS, is reached during the collapse. The collapse in

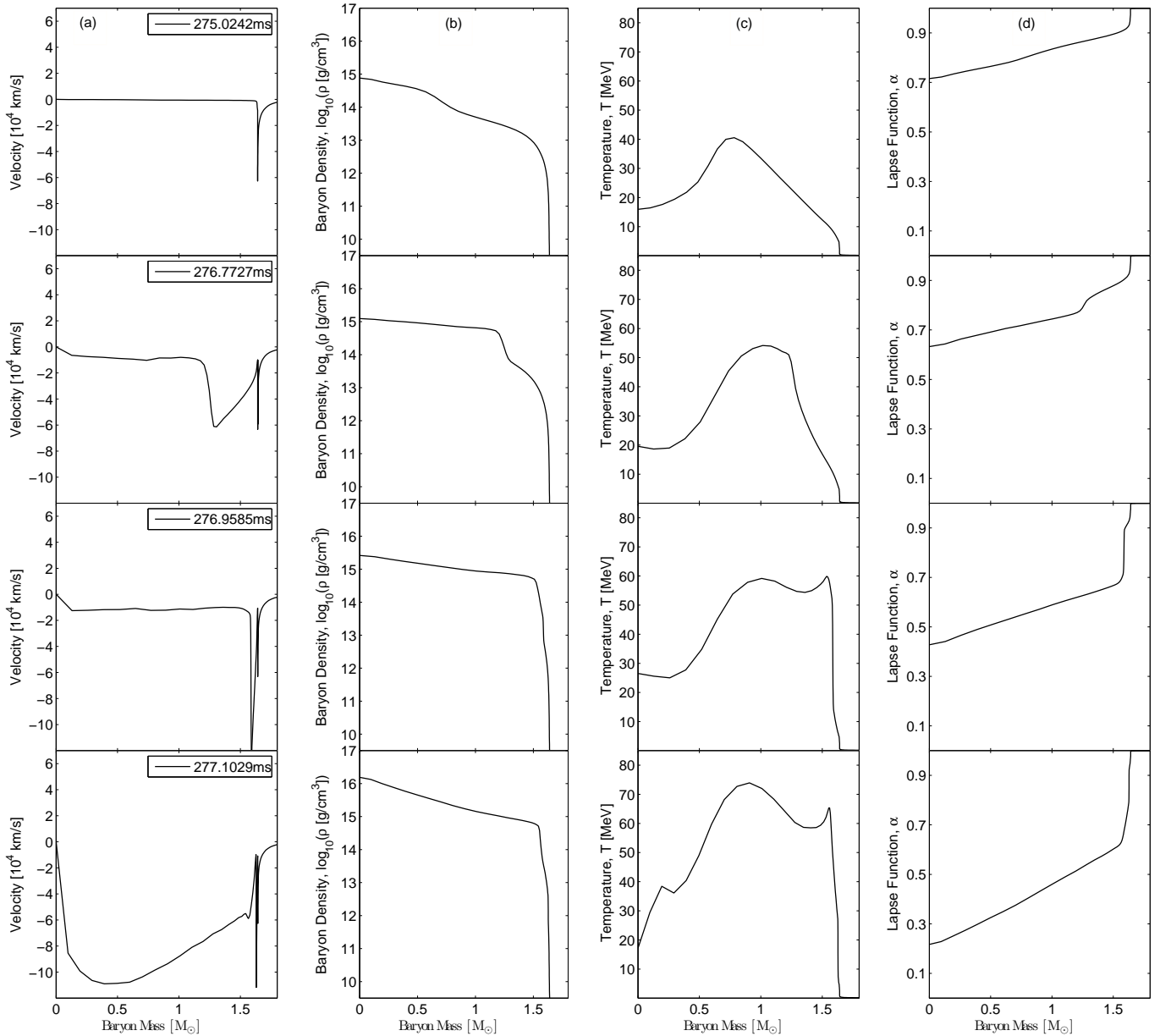


FIG. 18.— PNS collapse of the $15 M_{\odot}$ progenitor model using EOS2, at selected post bounce times during the PNS collapse, shock formation and shock propagation as well as the black hole formation.

turn is triggered due to the presence of quark matter in the interior. The inclusion of α_s -corrections in the hybrid EoS as introduced in §2.3 allows for more massive hybrid star configurations. It increases the maximum stable mass significantly. Applying the hybrid EOS3 ($B^{1/4} = 155$ MeV, $\alpha_s = 0.3$), leads to similar critical conditions for the onset of quark matter in comparison to EOS2, however with slightly higher critical density (see Table 2). Furthermore, the post bounce time for the PNS to become gravitationally unstable and collapse (see Table 2) is slightly delayed by about 50 ms (see Fig. 21), which results in slightly higher temperatures (see Table 2). The consequent evolutionary scenario is in qualitative agreement with the reference model as discussed in §. 3, i.e. the $10.8 M_{\odot}$ using EOS2. The remaining hybrid star has a baryon mass of about $1.65 M_{\odot}$ at the moment when the simulation is stopped. Due to the

larger maximum stable mass of the configuration, the PNS is found to be stable and does not collapse to a black hole.

The evolution of the corresponding neutrino luminosities and mean energies are shown in Fig. 21, which is in qualitative agreement with the spectra discussed for example of the reference model in §3.

4.5. PNS structure and the early evolution

The rise of the central density at the final phase of the Fe-core collapse of massive progenitor stars is shown in Fig. 22 (a) for the $10.8 M_{\odot}$ reference model. It reaches 10^{12} g/cm³ at about 6 ms before bounce and increases rapidly on a timescale on the order of milliseconds up to nuclear densities, on the order of $2 - 4 \times 10^{14}$ g/cm³. In general, the maximum values obtained for the central density depend on the EoS and on the progenitor

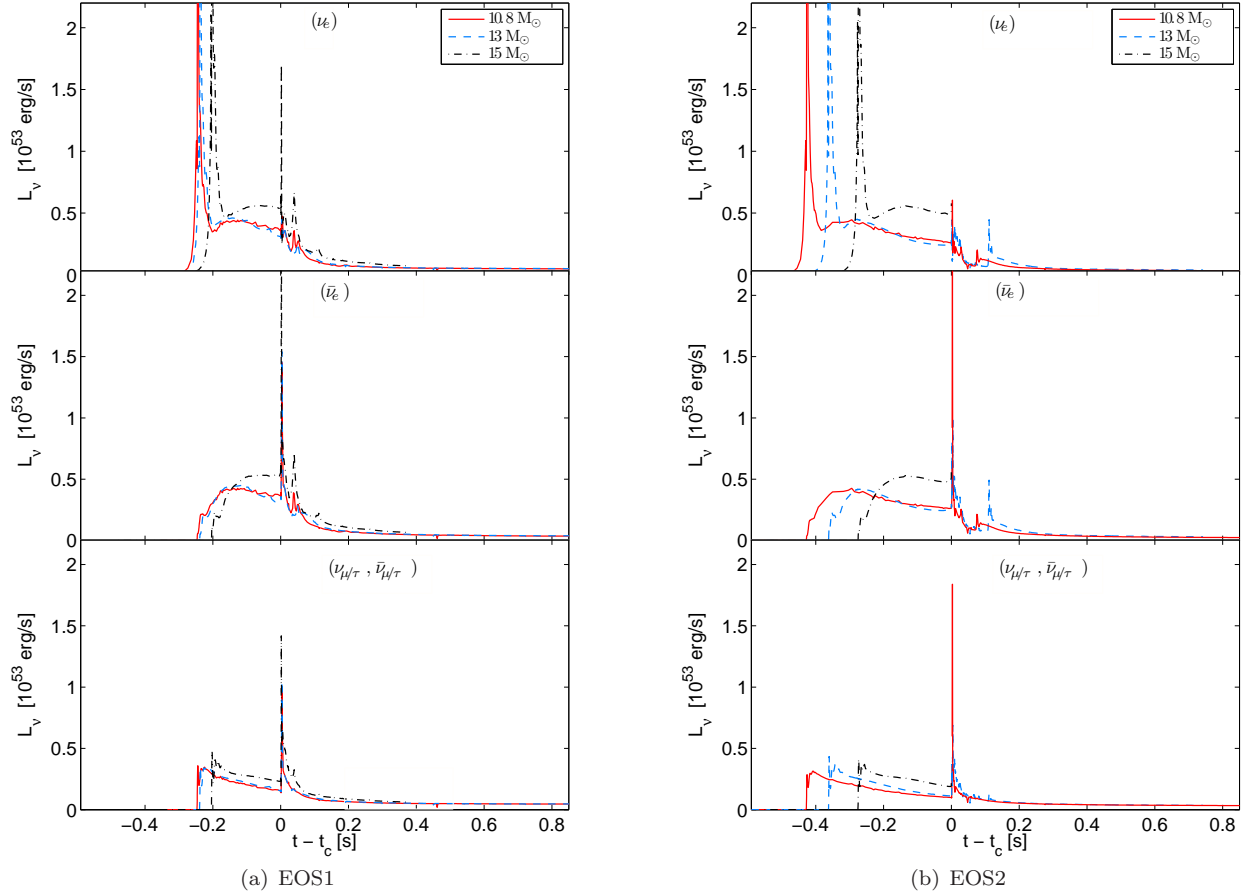


FIG. 19.— Neutrino luminosities for the different progenitor models under investigation. The time gauges t_c correspond to the moment when the maximum central densities are obtained for the different models during the PNS collapses.

TABLE 3
ESTIMATED NEUTRON STAR MASSES M_{NS} AND EXPLOSION ENERGIES E_{expl} AND THE MAXIMUM CENTRAL DENSITIES ρ_{max} FOR ALL MODELS UNDER INVESTIGATION.

Prog.	EoS	M_{NS}^a [M_{\odot}]	E_{expl}^a [10^{51} erg]	t_c^b [ms]	ρ_{max} [10^{15} g/cm 3]
10.8	EOS1	1.431	0.373	248.78	1.291
10.8	EOS2	1.479	1.194	429.81	1.806
13	EOS1	1.465	0.232	241.20	1.323
13	EOS2	1.496	0.635	364.06	1.788
15	EOS1	1.608	0.420	175.07	1.487
15	EOS2	1.641	unknown ^c	277.10 ^d	15.362 ^e
15	EOS3	1.674	0.458	312.99	1.342

^aNeutron star mass (baryon mass) and explosion energy, estimated at several 100 ms after the onset of explosion.

^bPost bounce times t_c ; correspond to the moments when the maximum central densities ρ_{max} are reached at the end of collapse

^cblack hole formation before positive explosion energy is achieved

^dtime of black hole formation

^ecentral density at the time of black hole formation

model. The moment of bounce, i.e. $t = 0$, is determined when the maximum central density is obtained (see Fig. 22 (a)). After bounce, the central density decreases slightly on the same short timescale on the order of milliseconds, until after about 10 ms post bounce the central density increases back again. It relates to the stalling of the bounce shock. After bounce, the central density stays above nuclear saturation density (see the

horizontal dotted line in Fig. 22). During the later post bounce evolution, which is determined by the presence of the standing accretion shock and hence mass accretion, the central density increases up to 6.3×10^{14} g/cm 3 at about 428 ms post bounce (see Fig. 22 (b)). At about 428.5357 ms post bounce, the PNS contraction proceeds into a collapse.

The density increases rapidly up to 1.29×10^{15} g/cm 3 (see Fig. 22 (b)). The post bounce time when the maximum central density is reached during the PNS collapse is labeled $t_c = 429.3$ ms. After t_c , the central density decreases again slightly, which relates to the initial expansion of the second shock wave formed inside the PNS. At about 0.1 ms after t_c , the central density starts to oscillate at a short timescale on the order of milliseconds, shown in Fig. 22 (b). This oscillation is due to the oscillating PNS interior, which is triggered by the mass accretion onto the outwards propagating accretion shock where nucleons are dissociated into quarks. Hence, the quark core continues to grow in mass. About 5 ms after t_c , the saturation value is obtained, where $\rho_{\text{central}} \simeq 1.25 \times 10^{15}$ g/cm 3 which remains constant with respect to time on the order of 100 ms. The central density will continue to rise only at later times and at a longer timescale, which is given by fall-back of material enclosed inside the mass cut and due to deleptonization (i.e. cooling).

The scenario explored here might reveal a connection between magnetars and neutron stars with quark matter

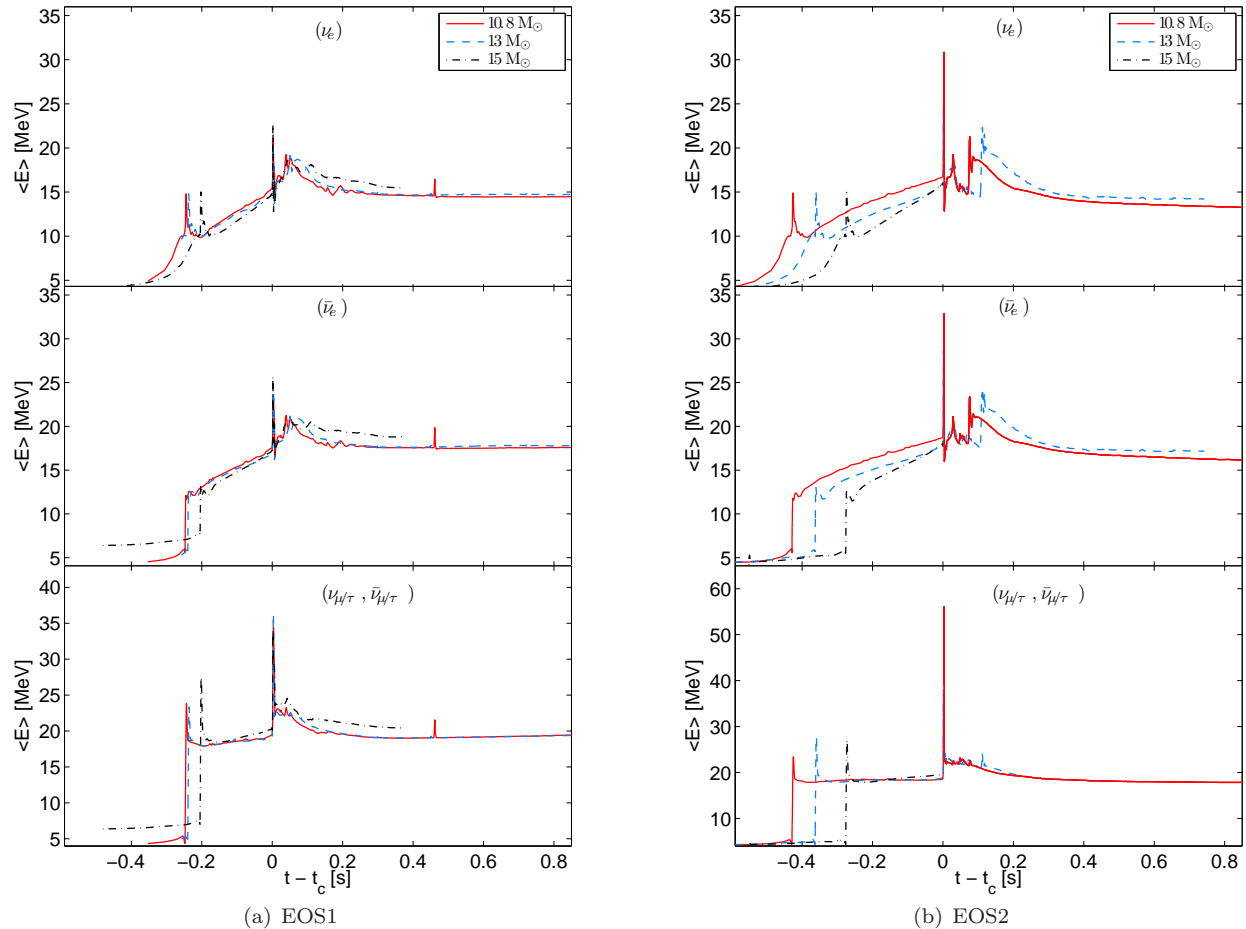


FIG. 20.— Mean neutrino energies for the different progenitor models under investigation. The same configuration as Fig. 19.

in the interiors. Due to flux conservation, the following relation between the baryon density ρ and the magnetic field strength B applies,

$$\frac{B_0}{B_1} = \left(\frac{\rho_0}{\rho_1} \right)^{\frac{2}{3}}. \quad (22)$$

This expression indicates a B -field increase during the Fe-core collapse post bounce as well as an additional B -field increase during the quark-hadron phase transition, in accordance with the density increase. The evolution of the central magnetic field, according to the above relation, is shown in Fig. 23 with respect to time after bounce. It corresponds to the density evolution shown in Fig. 22. Illustrated are three different initial magnetic field strengths, i.e. $B_0 = 10^9$ G, $B_0 = 10^{10}$ G and $B_0 = 10^{11}$ G. These are values which might be obtained at pre-collapse stellar models (see e.g. Heger & Langer 2000; Heger et al. 2005). At core bounce, for these initial configurations and according to the density evolution as discussed above, the central B -fields reach values of 10^{12} , 10^{13} and 10^{14} G. The post bounce compression increases the B -fields additionally by a factor of about 2 until the PNS collapses at about 428.3757 ms post bounce where, due to the density jump, the B -fields rise to about $2.5 \times 10^{12-14}$ G on a short timescale on the order of milliseconds. After the quark-hadron phase transition, the central density increases on a longer timescale on the

order of 100 ms up to seconds and hence the magnetic field strength increases slowly on the same timescale.

In addition to the evolution of the PNS interior in Fig. 23 for the central density evolution, close to the PNS surface the density decreases over several orders of magnitude. Hence we expect the magnetic field strengths at the PNS surface to be smaller in comparison to the evolution at the PNS center. Surprisingly, the B -fields reach values only slightly below 10^{12-14} G close to the PNS surface. During the later PNS evolution after the explosion has been launched, the PNS continues to contract. The subsequent density increase due to deleptonization on a longer timescale on the order of seconds, may cause an additional increase of the B -field where based on the three initial choices used values of 10^{15} G might be obtained at approximate simulation times on the order of 10 seconds post bounce.

In this ad-hoc approach, important effects such as the presence of rotation and fluid instabilities have been neglected. Due to angular momentum conservation, the PNS spins up during the (second) collapse. Even if at the onset of the (second) collapse the PNS is in solid-body rotation, the fact that the collapse proceeds non-homologously leads to differential rotation. Since a rotating body has the least rotational energy when it rotates solidly, there is some free energy stored in differential rotation. The free energy in differential rotation may be converted into magnetic energy by winding

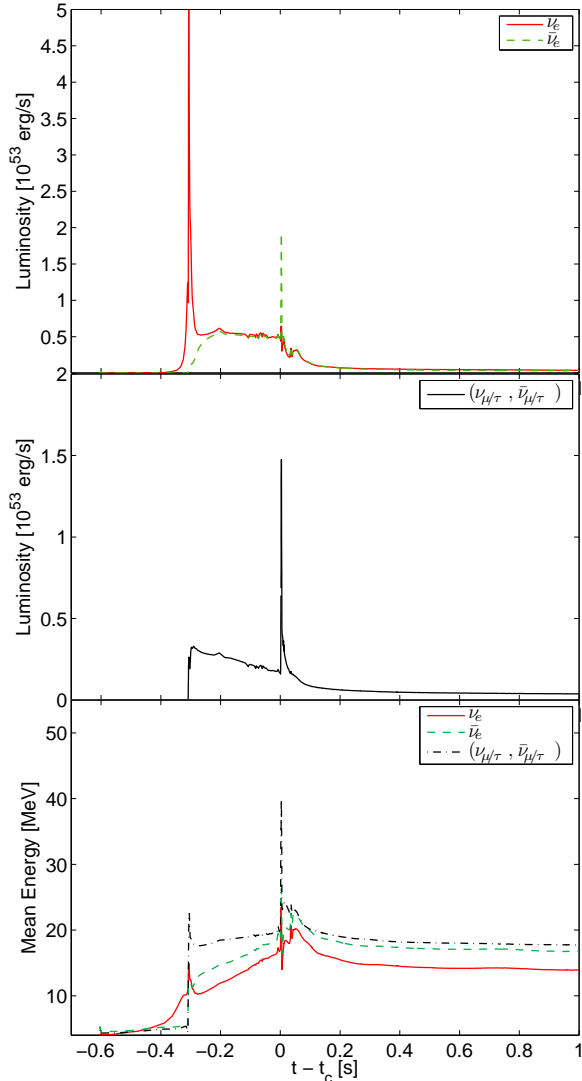
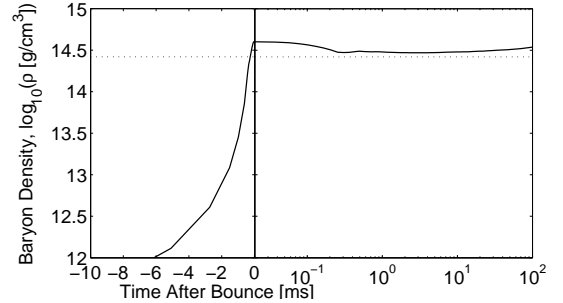


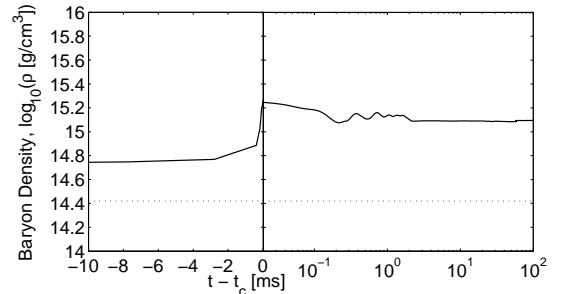
FIG. 21.— Luminosities and mean neutrino energies for the $15 M_{\odot}$ progenitor model using the hybrid EOS3. The time gauge t_c is again the moment when the maximum central density is obtained during the PNS collapse.

up poloidal field into toroidal field. Further, depending on the angular velocity profile, the PNS may also be subject to the magneto-rotational instability (MRI) (see Balbus & Hawley 1998). While field winding leads to a linear field strength growth, the MRI may lead to exponential field growth. Also convective motion from negative entropy and/or lepton gradients generated by the propagation of the second shock and the second neutrino burst may lead to dynamo action (see e.g. Thompson & Duncan 1993). Therefore our estimated values for the evolution of the magnetic field strength represent a lower limit. In order to obtain a more precise prediction of the magnetic field strength, detailed multidimensional investigations are necessary.

Finally, Fig. 24 schematically shows the resulting PNS structure, with quark matter in the interior. More precisely, the PNS is composed of an extended quark core surrounded by a high-density (including a reasonable amount of matter close to nuclear saturation density) hadronic mantle as well as a low-density envelope. The



(a) With respect to time after bounce.



(b) With respect to time after the PNS collapse when the maximum central density is obtained, i.e. $t_c = 429.81$ ms after bounce.

FIG. 22.— Evolution of the central density for the $10.8 M_{\odot}$ reference model with respect to time after bounce. The dotted line marks nuclear saturation density.

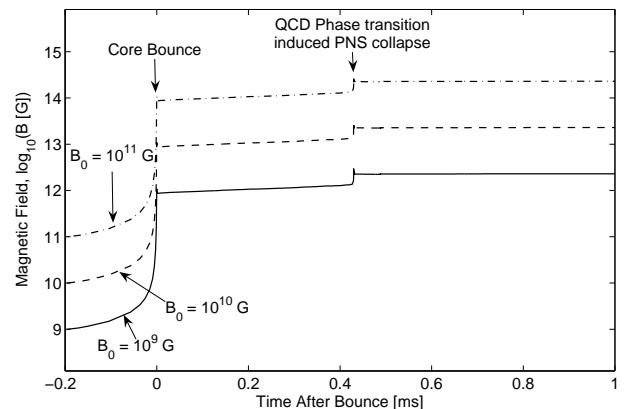


FIG. 23.— Evolution of the central magnetic field strength for the $10.8 M_{\odot}$ reference model with respect to time after bounce for three different initial magnetic field strengths (10^9 G, 10^{10} G, 10^{11} G).

surface of the PNS can be defined via the contracting neutrinospheres. The evolution of the PNS is determined by fall-back of very low-density hadronic material enclosed inside the mass cut. The mass cut estimate is a dynamical quantity which changes during the evolution. The mass enclosed inside the mass cut will form the remnant hybrid star. The remaining hybrid star cools after mass accretion vanishes, initially via deleptonization up to about one minute and later via photons up to millions of years. Matter outside the mass cut has become gravitationally unbound during the ongoing explosion and mass ejection from the PNS surface via neutrino heating (i.e. the neutrino-driven wind). This mass will be ejected into the interstellar medium. As can be seen from Fig. 24,

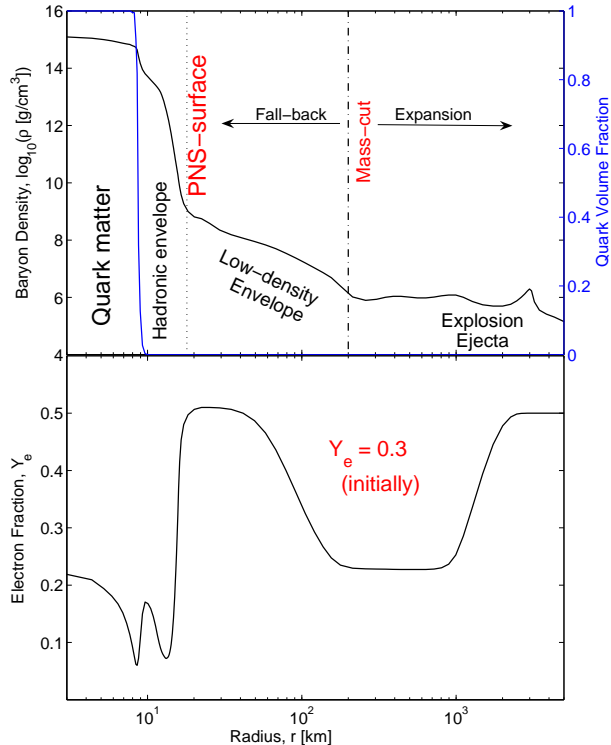


FIG. 24.— Schematic composition, illustrating the radial profile of the remaining hybrid PNS configuration for the reference $10.8 M_{\odot}$ progenitor model at late post bounce time.

a reasonable amount of mass (about $7 \times 10^{-3} M_{\odot}$) which corresponds to the ejected matter, has become neutron-rich with an electron fraction of $Y_e \simeq 0.3$. During the later expansion, the electron fraction increases and values between $Y_e \simeq 0.35-0.5$ are obtained. Detailed explosive nucleosynthesis investigations are required in order to confirm or exclude the scenario as a possible site for the synthesis of heavy elements via the r -process.

4.6. The explosion ejecta

The mass elements which are ejected directly (ballistically), are located at several 10^4 km during the Fe-core collapse, bounce and until the quark-hadron phase transition. They have densities and temperatures of several 10^6 g/cm³ and about 0.2 MeV, which remain constant with respect to time. These mass elements are relatively far away from the center and belong to the surrounding part of the Fe-core. The composition is dominated by ^{28}Si and ^{32}S , where $Y_e \simeq 0.5$. The structure of these layers is given by the progenitor model and changes only insignificantly during the collapse, bounce and early post bounce phases.

The situation changes when the expanding explosion shock crosses these mass elements. This happens at a post bounce time of about 450 ms for the $10.8 M_{\odot}$ reference model. The mass elements contract rapidly towards the PNS surface to about 10 km, during the PNS collapse. Density and temperature increase to several 10^{12} g/cm³ and several tens of MeV, on a short timescale on the order of milliseconds. Furthermore, the entropy per baryon increases from values below $10 k_B$ to about $60 k_B$ and the electron fraction decreases from $Y_e \simeq 0.5$ to $Y_e \simeq 0.1$. During the later expansion, density and temperature decrease initially on the same short timescale,

where a larger value for the electron fraction is obtained, between $Y_e \simeq 0.33-0.48$, and the entropy reduces to values close to $40 k_B$ per baryon. After the initial rapid expansion, these direct explosion ejecta expand on a longer timescale on the order of 100 ms up to seconds. Density and temperature decrease on the same timescale and reach values between 10^{3-4} g/cm³ and below 0.1 MeV at about 2 seconds post bounce. For these obtained conditions, the reaction rates become much smaller and hence the electron fraction changes on a longer timescale on the order of seconds. In addition, since the later expansion proceeds adiabatically, the entropy per baryon remains constant with respect to time as well, where values of $\simeq 40 k_B$ per baryon are obtained.

Mass elements which are not ejected directly in the initial shock expansion fall back onto the PNS surface at the center. During the short infall timescale on the order of milliseconds, density and temperature increase up to 10^{13} g/cm³ and 5–10 MeV. During the mass accretion onto the PNS surface, weak-equilibrium establishes at a low value of the electron fraction of $Y_e \simeq 0.05$ and the entropy per baryon decreases to values below $5 k_B$. However, after about 1.5 seconds post bounce the neutrino-driven wind appears as discussed in e.g. Arcones et al. (2007); Fischer et al. (2010b). One of the most important result of the appearance of the neutrino-driven wind relates to the high entropy conditions obtained for the accelerated matter. It results in generally proton-rich material, where $Y_e \simeq 0.55$ (first seen in Liebendörfer et al. (2003) and explained in Fröhlich et al. (2006) and Pruet et al. (2006)).

5. SUMMARY

We performed core-collapse supernova simulations of massive stars in the mass range of 10.8 to $15 M_{\odot}$, based on general relativistic radiation hydrodynamics employing a sophisticated EoS and three flavor Boltzmann neutrino transport. A description for three flavor quark matter is implemented based on the bag model with the different parameter choices, ($B^{1/4} = 162$ MeV, $\alpha_s = 0$ MeV), ($B^{1/4} = 165$ MeV, $\alpha_s = 0$ MeV) and ($B^{1/4} = 155$ MeV, $\alpha_s = 3$ MeV). The resulting quark EoSs, EOS1, EOS2 and EOS3, are coupled to the hadron EoS from Shen et al. (1998), where Gibbs conditions are applied for the transition between hadron and quark matter. It results in an extended co-existence region in the phase diagram where nucleons and quarks are present, the mixed phase. The thermodynamic conditions for the appearance of quark matter relate to critical densities close to nuclear matter density, for temperatures of tens of MeV and a low proton-to-baryon ratio.

During the evolution of massive stars, we find that quark matter appears already at the Fe-core bounce for the chosen parameters. However, the quark matter volume fraction is found to be rather small with $\chi \leq 0.1$. The quark matter volume fraction increases slowly over several 100 ms during the early post bounce mass accretion phase, during which central density and temperature increase while the central electron fraction decreases. The EoS in the mixed phase is significantly softer compared to the pure hadronic and the pure quark phases. Hence, the PNS contraction accelerates during the post bounce evolution as more and more matter of the PNS in-

terior is converted into the mixed phase. Finally, the central PNS configuration becomes gravitationally unstable and the contraction proceeds into an adiabatic collapse. Density and temperature increase on a short timescale on the order of milliseconds, which in turn favors quark matter over hadronic matter. The stiffening of the EoS in the pure quark phase halts the collapse and a strong hydrodynamic shock wave forms. The shock appears initially as a pure accretion front. It propagates outward along the decreasing density of the PNS. The propagation is determined via the balance of ram pressure from the supersonically infalling material ahead of the shock and the thermal pressure of the quarks as well as neutrino heating behind the shock. At the PNS surface where the density decreases over several orders of magnitude, the accretion shock accelerates and positive matter velocities are obtained. The accretion front turns into a dynamic shock wave, which continues to expand. This moment establishes the onset of explosion. It finally merges with the standing accretion shock from the Fe-core bounce, which remained unaffected from the happenings inside the PNS. All models under investigation follow the same evolutionary behavior and lead to explosions, if the PNS mass does not exceed the maximum stable mass of the configuration given by the hybrid EoS.

Investigating the large uncertainty in core-collapse supernova input physics, i.e. the state of matter at high densities and temperatures and with a low proton-to-baryon ratio, we were able to explore a new explosion mechanism in simulations of massive stars. It serves as an addition to the well explored neutrino-driven, the magnetically-driven and the acoustic mechanisms. Note that these appear to be working only in multiple spatial dimensions (except for the low mass O-Ne-Mg-core), due to the nature of the physics directly involved in these explosion mechanisms. The explosions obtained by taking QCD degrees of freedom into account are presumably not restricted to dimensional limitations. However, moderate explosion energies on the order of 10^{51} erg could only be obtained for the $10.8 M_{\odot}$ progenitor model and for a particular choice of parameters. Taking multi-dimensional phenomena into account, such as rotation and the development of fluid instabilities, may shift the explosion energies to robust values.

The sudden density rise during the seconds collapse indicates an additional increase of the magnetic field strength. It enables us to give a lower estimate of the expected magnetic field strength for protoneutron stars with quark matter cores. However, with initial magnetic fields that are confirmed by stellar evolution calculations, a connection between hybrid stars and the special neutron star class *Magnetars* with magnetic fields up to several 10^{15} G could not be established. Important aspects of the magneto-hydrodynamics evolution have not been taken into account due to the current restriction to spherical symmetry. They will be explored in a detailed study in an upcoming article.

Direct observables which allow us to identify the appearance of quark matter in the PNS interior cannot be expected in the neutrino signal, because matter is opaque for neutrinos. Neutrinos can only diffuse out of the PNS interior on timescales on the order of seconds. However, the presence of a strong hydrodynamic shock wave changes the situation. It releases an additional outburst

of neutrinos when crossing the neutrinospheres. This millisecond neutrino burst is dominated by $\bar{\nu}_e$, because matter is neutron-rich where positron captures dominate over electron captures, and by similar fluxes of ν_e and $(\nu_{\mu/\tau}, \bar{\nu}_{\mu/\tau})$ that are produced via pair process. The delay of the second neutrino burst to the deleptonization burst from the Fe-core bounce and its magnitude, contain information about the progenitor model, the hadronic and quark EoSs, including the critical conditions for the onset of quark matter as well as the nature of the phase transition from hadronic matter to quark matter. It will become observable for future Galactic events, as confirmed recently by Dasgupta et al. (2010) for the operating neutrino detectors Super-Kamiokande and IceCube. The knowledge of the progenitor model and the hadronic EoS may allow us to decode hidden information about the state of matter at high densities and temperatures, conditions which will likely be reached in future heavy-ion collision experiments at FAIR/GSI (Germany) and NICA/Dubna (Russia). Furthermore, direct observables from the quark-hadron phase transition can be expected in the emission of gravitational waves. These might become observable in the near future if the sensitivity improvements of the gravitational wave detectors continue. They will serve as important addition to the neutrino spectra.

The composition of the ejecta can also be used to probe the explosion scenario. Although core-collapse supernovae have been considered as the favored site for possible r -process nucleosynthesis for a long time, the required conditions have not been found in simulations so far. Therefore it would be interesting to explore whether an r -process can ensue in the layers being ejected here. We defer, however, a thorough investigation to a separate paper. The reduced nuclear reaction network included here to account for energy generation is not suited to follow the Y_e evolution and nucleosynthesis at late times. Nevertheless, there is only a small range of layers to be considered. Neutron-rich matter from the deep layers close to the PNS surface attains $Y_e \simeq 0.33-0.48$ after shock heating and is ejected ballistically. Layers in a second class are not directly ejected, rather they fall back onto the PNS surface, where they experience continued neutrino heating and can subsequently be ejected. Initially, these layers can be very neutron-rich but turn proton-rich as they expand in the neutrino-wind developing at later times. Therefore, only the directly ejected zones may contain viable conditions for neutron-rich nucleosynthesis, provided they are located not too far above the PNS surface.

With this study we address a deeper understanding of the inclusion of QCD degrees of freedom in radiation hydrodynamics studies of astrophysical scenarios, explored at the example of core-collapse supernova simulations of massive stars. The quark matter description applied here leads to an early onset of the chiral phase transition. This is an active subject of research where several aspects, such as the chiral phase transition in general, the hadronic freeze out, the existence of a possible quarkyonic phase (McLerran & Pisarski 2007) and the nature of the transition between hadronic and quark matter, are investigated. Further developments of quark matter EoSs where different conditions with respect to the critical conditions for the onset of deconfinement may favor

different evolutionary scenarios, will be studied in the future. Furthermore, simulations in multiple spatial dimensions are required in order to support the findings of the present article.

ACKNOWLEDGMENTS

The project was funded by the Swiss National Science Foundation grant. no. PP00P2-124879/1 and 200020-122287 and the Helmholtz Research School for Quark Matter Studies, and the Helmholtz International Center (HIC) for FAIR. T.F. is supported by HIC for FAIR project no. 62800075 and G.M.P. is partly supported by the Sonderforschungsbereich 634, the ExtreMe Matter Institute EMMI and HIC for FAIR. I.S. is supported by the Alexander von Humboldt foundation via the

Feodor-Lynen fellowship and the work of G.P. is supported by the Deutsche Forschungsgemeinschaft (DFG) under Grant No. PA 1780/2-1. J.S.-B. is supported by the DFG through the Heidelberg Graduate School of Fundamental Physics. M.H. acknowledges support from the High Performance and High Productivity Computing (HP2C) project. The authors are additionally supported by CompStar, a research networking program of the European Science Foundation, and the Scopes project funded by the Swiss National Science Foundation grant. no. IB7320-110996/1. The authors would also like to thank Dr. Mary Beard from the University of Notre Dame for proofreading the manuscript with focus on the English language.

REFERENCES

- Alford, M., Braby, M., Paris, M. & Reddy, R. 2005, *ApJ*, 629, 969
- Alford, M., Blaschke, D., Drago, A., Klähn, T., Pagliara, G. & Schaffner-Bielich, J. 2007, *Nature*, 445,
- Amsler, C. et al. 2008, *Physics Letters B*, 667
- Aoki, Y., Endrodi, G., Fodor, Z., Katz, S. D. & Szabo, K. K. 2006, *Nature*, 443, 675
- Arcones, A., Janka, H.-Th. & Scheck, L. 2007, *A&A*, 467, 1227
- Balbus, S. A. & Hawley, J. F. 1998, *Reviews of Modern Physics*, 70, 1
- Bauswein, A. et al. 2009, *Phys. Rev. Lett.*, 103, 011101
- Berges, J. & Rajagopal, K. 1999, *Nucl. Phys. B*, 538, 215
- Bethe, H. A. & Wilson, J. R. 1985, *ApJ*, 295, 14
- Bionta, R. M., Blewitt, G., Bratton, C. B., Caspere, D. & Ciocio, A. 1987, *Phys. Rev. Lett.*, 58, 1494
- Bogolyubov, P. N. 1968, *Annales Poincaré Phys. Theor.*, 8, 163
- Bruenn, S. W. 1985, *ApJS*, 58, 771
- Bruenn, S. W. 1989, *ApJ*, 340, 995
- Bruenn, S. W., Mezzacappa, A., Hix, W. R., Blondin, J. M., Marronetti, P., Messer, O. E. B., Dirk, C. J. & Yoshida, S. 2009, *Journal of Physics Conference Series*, 180, 012018
- Buballa, M. 2005, *Phys. Report*, 407, 205
- Bugaev, K. A.; Gorenstein, M. I.; Kmpfer, B. & Zhdanov, V. I. 1989 *Phys. Rev. D*, 40, 2903
- Buras, R., Janka, H.-Th., Keil, M. Th., Raffelt, G. G. & Rampp, M. 2003, *ApJ*, 587, 320
- Burrows, A., Hayes, J. & Fryxell, B. A. 1995, *ApJ*, 450, 830
- Burrows, A., Livne, E., Dessart, L., Ott, C. D. & Murphy, J. 2006, *ApJ*, 655, 416
- Chodos, A., Jaffe, R. L., Johnson, K., Thorn, C. B. & Weisskopf, V. F. 1974b, *Phys. Rev. D*, 9, 3471
- Dasgupta, B., Fischer, T., Horiuchi, S., Liebendörfer, M., Mirizzi, A., Sagert, I. & Schaffner-Bielich, J. 2010, *Phys. Rev. D*, 81, 103005
- Degrand, T., Jaffe, R. L., Johnson, K. & Kiskis, J. 1975, *Phys. Rev. D*, 12, 2060
- Demorest, P. B., Pennucci, T., Ransom, S. M., Roberts, M. S. E. & Hessels, J. W. T. 2010, *Nature*, 467, 1081
- Detar, C. E. & Donoghue, J. F. 1983, *Annual Review of Nuclear and Particle Science*, 33, 235
- Drago, A. & Tambini, U. 1999, *Journal of Physics G: Nuclear Physics*, 25, 971
- Farhi, E. & Jaffe, R. L. 1984, *Phys. Rev. D*, 30, 2379
- Fischer, C. S. 2006, *Journal of Physics G: Nuclear Physics*, 32, 253
- Fischer, T., Whitehouse, S. C., Mezzacappa, A., Thielemann, F.-K. & Liebendörfer, M. 2009, *A&A*, 499, 1
- Fischer, T., Sagert, I., Hempel, M., Pagliara, G., Schaffner-Bielich, J. & Liebendörfer, M. 2010, *Class. Quant. Grav.*, 27, 114102
- Fischer, T., Whitehouse, S. C., Mezzacappa, A., Thielemann, F.-K. & Liebendörfer, M. 2010, *A&A*, 517, A80
- Fodor, Z. & Katz, S. D. 2004, *Journal of High Energy Physics*, 4, 50
- Freiburghaus, C., Rembges, J.-F., Rauscher, T., Kolbe, E., Thielemann, F.-K., Kratz, K.-L., Pfeiffer, B. & Cowan, J. J. 1999, *ApJ*, 516, 381
- Freire, P. C. C., Wolszczan, A., van den Berg, M. & Hessels, J. W. T. 2008, *ApJ*, 679, 1433
- Freire, P. C. C. & Wex, N. 2010, print (astro-ph/1006.0642)
- Fröhlich, C., Martínez-Pinedo, G., Liebendörfer, M., Thielemann, F.-K., Bravo, E., Hix, W.-R., Langanke, K. & Zinner, N. T. 2006, *Phys. Rev. Lett.*, 96, 142502
- Gentile, N. A., Aufderheide, M. B., Mathews, G. J., Swesty, F. D. & Fuller, G. M. 1993, *ApJ*, 414, 701
- Glendenning, N. 1996, *Compact Stars. Nuclear Physics, Particle Physics and General Relativity* (Springer-Verlag New York)
- Heger, A. & Langer, N. 2000, *ApJ*, 544, 1016
- Heger, A., Woosley, S. E. & Spruit, H. C. 2005, *ApJ*, 626, 350
- Hempel, M., Pagliara, G. & Schaffner-Bielich, J. 2009, *Phys. Rev. D*, 80, 125014
- Hempel, H. & Schaffner-Bielich, J. 2010, *Nuclear Physics A*, 837, 210
- Herant, M., Benz, W., Hix, W. R., Fryer, C. L. & Colgate, S. A. 1994, *ApJ*, 435, 339
- Heuze, O., Jaouen, S. & Jourdain, H. 2008 *Journal of Computational Physics*, 228, 833
- Hirata, K. S. et al. 1988, *Phys. Rev. D*, 38, 448
- Hillebrandt, W. & Müller, E. 1981, *A&A*, 103, 147
- Iosilevskiy, I. 2010, *Acta Physica Polonica B Proceedings Supplement*, 3, 589
- Ishizuka, C., Ohnishi, A., Tsubakihara, K., Sumiyoshi, K. & Yamada, S. 2008, *Journal of Physics G: Nuclear Physics*, 35, 085201
- Janka, H.-Th. & Mueller, E. 1996, *A&A*, 306, 167
- Janka, H.-Th. 2001, *A&A*, 368, 527
- Kitaura, F. S., Janka, H.-Th. & Hillebrandt, W. 2006, *A&A*, 450, 345
- Klevansky, S. P. 1992, *Reviews of Modern Physics*, 64, 649
- Klebanov, I. R. & Witten, E. 1999, *Nuclear Physics B*, 556, 89
- Kolb, P. F., Sollfrank, J. & Heinz, U. 2000, *Phys. Rev. C*, 62, 054909
- Kurkela, A., Romantschke, P., Vuorinen, A. & Wu, B. 2010, preprint (astro-ph/1006.4062)
- Lattimer, J. M. & Swesty, D. F. 1991, *Nuclear Physics A*, 535, 331
- LeBlanc, J. M. & Wilson, J. R. 1970, *ApJ*, 161, 541
- Li, B.-A., Chen, L.-W. & Ko, C. M. 2008, *Physics Reports*, 464, 113
- Liebendörfer, M., Mezzacappa, A. & Thielemann, F.-K., 2001a, *Phys. Rev. D*, 63, 104003
- Liebendörfer, M., Rosswog, S. and Thielemann, F.-K., Messer, O. E. B., Hix, W. R. & Bruenn, S. W. 2001b, *Phys. Rev. D*, 63, 103004
- Liebendörfer, M., Rosswos, S. & Thielemann, F.-K., 2002, *ApJS*, 141, 229
- Liebendörfer M., Mezzacappa, A., Messer, O. E. B., Martínez-Pinedo, G., Hix, W. R. & Thielemann, F.-K. 2003, *Nuclear Physics A*, 719, 144

- Liebendörfer, M., Messer, O. E. B., Mezzacappa, A., Bruenn, S. W., Cardall, C. Y. & Thielemann, F.-K. 2004, *ApJS*, 150, 263
- Liebendörfer, M., Ramp, M, Janka, H.-Th. & Mezzacappa, A. 2005, *ApJ*, 620, 840
- Marek, A. & Janka, H.-Th. 2009, *ApJ*, 694, 664
- Mayle, R. & Wilson, R. 1987, *ApJ*, 318, 288
- McLerran, L. & Pisarski, R. D. 2007, *Nuclear Physics A*, 796, 83
- Mezzacappa, A. & Bruenn, S. W. 1993a, *ApJ*, 405, 637
- Mezzacappa, A. & Bruenn, S. W. 1993b, *ApJ*, 405, 669
- Mezzacappa, A. & Bruenn, S. W. 1993c, *ApJ*, 410, 740
- Mezzacappa, A. & Messer, O. E. B. 1999, *Journal of Computational and Applied Mathematics*, 109, 281
- Miller, D. S., Wilson, J. R. & Mayle, R. W. 1993, *ApJ*, 415, 278
- Moiseenko, S. G. & Bisnovatyi-Kogan, G. S. 2007, *Ap&SS*, 311, 191
- Müller, H. & Serot, B. D. 1995, *Phys. Rev. C*, 52, 2072
- Myra, E. S. & Bludman, S. A. 1989, *ApJ*, 340, 384
- Nakazato, K., Sumiyoshi, K. & Yamada, S. 2008a, *Phys. Rev. D*, 77, 103006
- Nakazato, K., Sumiyoshi, K., Suzuki, H. & Yamada, S. 2008b, *Phys. Rev. D*, 78, 083014
- Nakazato, K., Sumiyoshi, K., Suzuki, H. & Yamada, S. 2010a, *Phys. Rev. D*, 81, 083009
- Nakazato, K., Sumiyoshi, K. & Yamada, S. 2010b, *ApJ*, 721, 1284
- Nomoto, K. 1983, *IAU Symposium*, 101, 139
- Nomoto, K. 1984, *ApJ*, 277, 791
- Nomoto, K. 1987, *ApJ*, 322, 206
- Ozel, F., Psaltis, D., Ransom, S., Demorest, P. & Alford, M. 2010, *ApJ*, 724, L199
- Pagliara, G., Hempel, M. & Schaffner-Bielich, J. 2009, *Phys. Rev. Lett.*, 103, 171102
- Pagliara, G. & Schaffner-Bielich, J. 2010, *Phys. Rev. D*, 81, 094024
- Pisarski, R. D. & Wilczek, F. 1984, *Phys. Rev. D*, 29, 014019
- Pruet, J., Hoffman, R. D., Woosley, S. E., Janka, H.-T. & Buras, R. 2006 *ApJ*, 644, 1028
- Rampp, M. & Janka, H.-Th. 2000, *ApJ*539, L33
- Ratti, C., Thaler, M. A. & Weise, W. 2006, *Phys. Rev. D*, 73, 014019,
- Rauscher, T., Applegate, J. H., Cowan, J. J., Thielemann, F.-K. & Wiescher, M. 1994, *ApJ*, 429, 499
- Rischke, D. H., Friman, B. L., Waldhauser, B M., Stcker, H. & Greiner, W. 1990, *Phys. Rev. D*, 41, 111
- Sagert, I., Fischer, T., Hempel, M., Pagliara, G., Schaffner-Bielich, J., Mezzacappa, A., Thielemann, F.-K. & Liebendörfer, M. 2009, *Phys. Rev. Lett.*, 102, 081101
- Sagert, I., Fischer, T., Hempel, M., Pagliara, G., Schaffner-Bielich, J., Thielemann, F.-K. & Liebendörfer, M. 2010, *Journal of Physics G Nuclear Physics*, 37, 094064
- Sagert, I., Schaffner-Bielich, J. & Sturm, C. 2010, *Work in progress*
- Schertler, K., Greiner, C., Schaffner-Bielich, J. & Thomas, M. H. 2000, *Nuclear Physics A*, 677, 463
- Shen, H., Toki, H., Oyamatsu, K. & Sumiyoshi, K. 1998, *Nuclear Physics A*, 637, 435
- Shuryak, E. V. & Zahed, I. 2004, *Phys. Rev. C*, 70, 021901
- Steiner, A. W., Lattimer, J. M. & Brown, E. F. 2010, *ApJ*, 722, 33
- Steiner, A. W., Prakash, M. & Lattimer, J. M. 2010, *Physics Letters B*, 486, 239
- Sumiyoshi, K., Yamada, S. & Suzuki, H. 2007, *ApJ*, 667, 382
- Takahara, M. & Sato, K. 1988, *ApJ*, 335, 301
- Takiwaki, T., Kotake, K. & Sato, K. 2009, *ApJ*, 691, 1360
- Thielemann, F.-K., Brachwitz, F., Höflich, P., Martínez-Pinedo, G. & Nomoto, K. 2004, *New Astronomy Review*, 48, 605
- Thompson, C. & Duncan, R. C. 1993, *ApJ*, 408, 194
- Thompson, T. A. & Burrows, A. 2001, *Nuclear Physics A*, 688, 377
- Thompson, T. A., Burrows, A. & Pinto, P. A. 2003, *ApJ*, 592, 434
- Timmer, F. X. & Arnett, D. 1999, *ApJS*, 125, 277
- Weber, F. 1999, *Pulsars as Astrophysical Laboratories for Nuclear and Particle Physics (Bristol, U.K. : Institute of Physics)*
- Weissenborn, S., Sagert, I., Pagliara, G., Hempel, M. & Schaffner-Bielich, J. 2011, *print (astro-ph/1102.2869)*
- Witten, E., 1984, *Phys. Rev. D*, 30, 272
- Woosley, S. E. & Weaver, T. E. 1995, *ApJS*, 101, 181
- Woosley, S. E., Heger, A. & Weaver, T. E. 2002, *Reviews of Modern Physics*, 74, 1015
- Yasutake, N., Maruyama, T. & Tatsumi, T. 2009, *Phys. Rev. D*, 80, 123009

